

Supplementary Materials for  
**Structure and function of otoferlin, a synaptic protein of sensory hair cells  
essential for hearing**

Han Chen *et al.*

Corresponding author: Tobias Moser, [tmoser@gwdg.de](mailto:tmoser@gwdg.de); Julia Preobraschenski,  
[julia.preobraschenski@med.uni-goettingen.de](mailto:julia.preobraschenski@med.uni-goettingen.de)

*Sci. Adv.* **11**, eady8532 (2025)  
DOI: 10.1126/sciadv.ady8532

**The PDF file includes:**

Figs. S1 to S15  
Tables S1 to S4  
Legends for movies S1 to S4  
References

**Other Supplementary Material for this manuscript includes the following:**

Movies S1 to S4

**Figure S1**

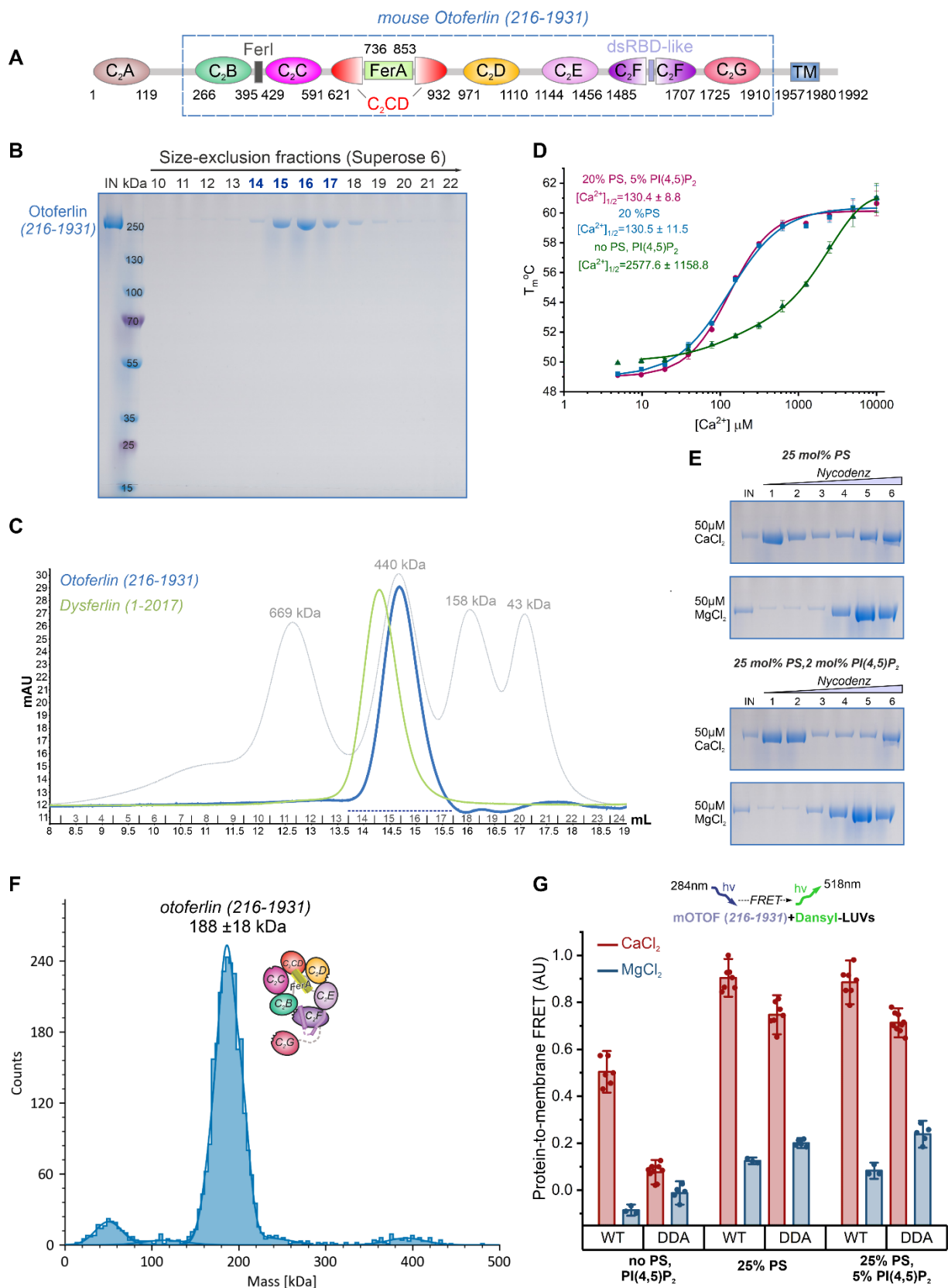


### Figure S1. Biochemical characterization of mouse otoferlin

(A) Structure-based domain composition schematic of mouse otoferlin. The borders of the otoferlin construct (residues 216-1931) used for cryo-EM structure determination are boxed.

(B) SDS-PAGE analysis of purified mouse otoferlin (residues 216-1931) after size-exclusion chromatography (SEC).

(C) The SEC profile of mouse otoferlin (216-1931) applied to a Superose 6 column. The peak otoferlin fractions (see also B) are indicated with a dashed line and soluble dysferlin (residues 1-2017) was used as a ferlin mass reference. The SEC profile of several gel filtration standards with known molecular masses are shown in grey.

(D)  $\text{Ca}^{2+}$ -binding activity of otoferlin (216-1931) assessed in the presence of liposomes. The  $\text{Ca}^{2+}$ -binding activity was assessed using a nanoDSF assay and large unilamellar vesicles (LUVs) of indicated composition (comprising 20 mol% PS, 20 mol% PS and 5 mol% PI(4,5) $\text{P}_2$  or lacking anionic phospholipids, no PS, PI(4,5) $\text{P}_2$ ) were used at a 1 mM assay concentration.  $[\text{Ca}^{2+}]_{1/2}$  values were estimated by nonlinear regression curve fit. Error bars represent the standard error of the mean (SEM,  $n=3$ ).

(E)  $\text{Ca}^{2+}$ -sensitive liposome binding activity of mouse otoferlin (216-1931) assessed using a coflotation assay. Binding of otoferlin to LUVs of indicated acidic phospholipids composition was assessed by ultracentrifugation on a Nycodenz step in the presence of 50  $\mu\text{M}$   $\text{CaCl}_2$  or  $\text{MgCl}_2$ . The Nycodenz gradients were harvested from the top, analyzed by SDS-PAGE, and stained with Coomassie Blue.

(F) Characterization of the soluble otoferlin (216-1931) construct by mass photometry. The distribution of binding events is consistent with the presence of a major otoferlin (216-1931) species having a molecular mass of  $188 \pm 18$  kDa. The measurements were carried out in the absence of  $\text{CaCl}_2$  and were repeated four times ( $n=4$ ).

(G) Liposome binding activity of mOTOF (216-1931) and mOTOF (216-1931)-D1829A/D1831A (DDA) mutant using a FRET-based assay. The measurements were carried out in the presence of 250  $\mu\text{M}$   $\text{CaCl}_2$  or  $\text{MgCl}_2$  at 0.25  $\mu\text{M}$  and 50  $\mu\text{M}$  protein and liposome concentrations, respectively. The measured LUVs comprised 5 mol% Dansyl-PE. The measurements in the presence of  $\text{CaCl}_2$  were repeated  $n=6$  (WT, in the presence of liposomes lacking PS and PI(4,5) $\text{P}_2$ , denoted as no PS, PI(4,5) $\text{P}_2$ ),  $n=9$  (DDA, in the presence of liposomes comprising 25 mol% PS and 5 mol% PI(4,5) $\text{P}_2$  or lacking PS and PI(4,5) $\text{P}_2$ ), or  $n=7$  (remaining measurements). The measurements in the presence of  $\text{MgCl}_2$  were carried out in  $n=3$  (WT) or  $n=5$  (DDA) replicates. The data were normalized to the maximum Dansyl-PE emission after subtraction of the background at each individual point (using protein-free measurements) and error bars indicate the standard deviation (SD) from the mean ( $\pm 1.5$  SD). See also Figure 3G.

**Figure S2**

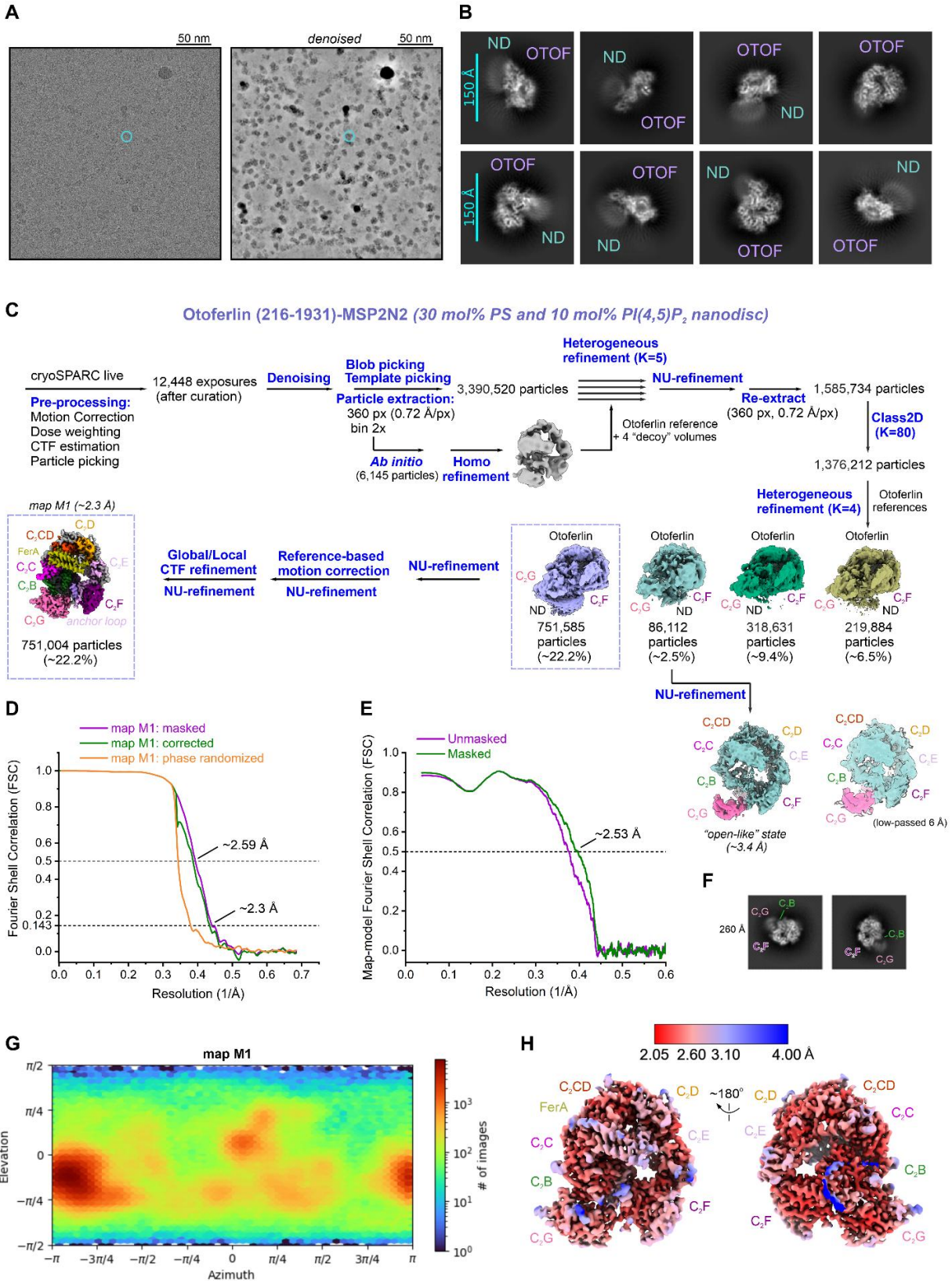


**Figure S2. Cryo-EM image analysis of the otoferlin (216-1931)-nanodisc complex  
(30 mol% PS and 10 mol% PI(4,5)P<sub>2</sub> MSP2N2 nanodisc)**

(A) Cryo-EM micrograph (raw and denoised) of the vitrified otoferlin (216-1931)-MSP2N2 complex. The MSP2N2 nanodisc comprised of 30 mol% DOPS and 10 mol% PI(4,5)P<sub>2</sub>. A typical otoferlin particle is circled.

(B) Reference-free 2D class averages of the otoferlin (216-1931)-MSP2N2 nanodisc complex. The nanodisc-bound bound otoferlin (OTOF) and the nanodisc (ND) are indicated. The images of the 2D class averages were generated using the freely available cryosparc-tools Python package (<https://tools.cryosparc.com/>).

(C) Cryo-EM processing routine of otoferlin (216-1931)-MSP2N2 nanodisc complex (30 mol% DOPS and 10 mol% PI(4,5)P<sub>2</sub> nanodisc). The resolution estimates (FSC=0.143 criterion) of the final maps are indicated, and the final maps are coloured according to the modelled domains (see also Fig. S1A).

(D) Fourier shell correlation (FSC) plots between the otoferlin-MSP2N2 cryo-EM half-maps. The global resolution of the map (map M1) was estimated using the gold-standard FSC criterion (FSC=0.143).

(E) Map versus model FSC plot for the map M1 of the otoferlin (216-1931)-MSP2N2 complex (30 mol% DOPS and 10 mol% PI(4,5)P<sub>2</sub>).

(F) Reference-free 2D class averages of lipid-bound otoferlin particles assigned to the “open-like” conformational state. In this “open-like” state, observed for ~2.5% of otoferlin-nanodisc particles, C<sub>2</sub>G is dynamic and does not interact with the C<sub>2</sub>B domain.

(G) Angular distribution of the otoferlin-MSP2N2 particles contributing to the map M1 of the complex. Red colour indicates a higher number of particle images.

(H) Local resolution of the lipid-bound otoferlin cryo-EM map (map M1). Red colour indicates a higher resolution of the map. The otoferlin domains are indicated.



**Figure S3**

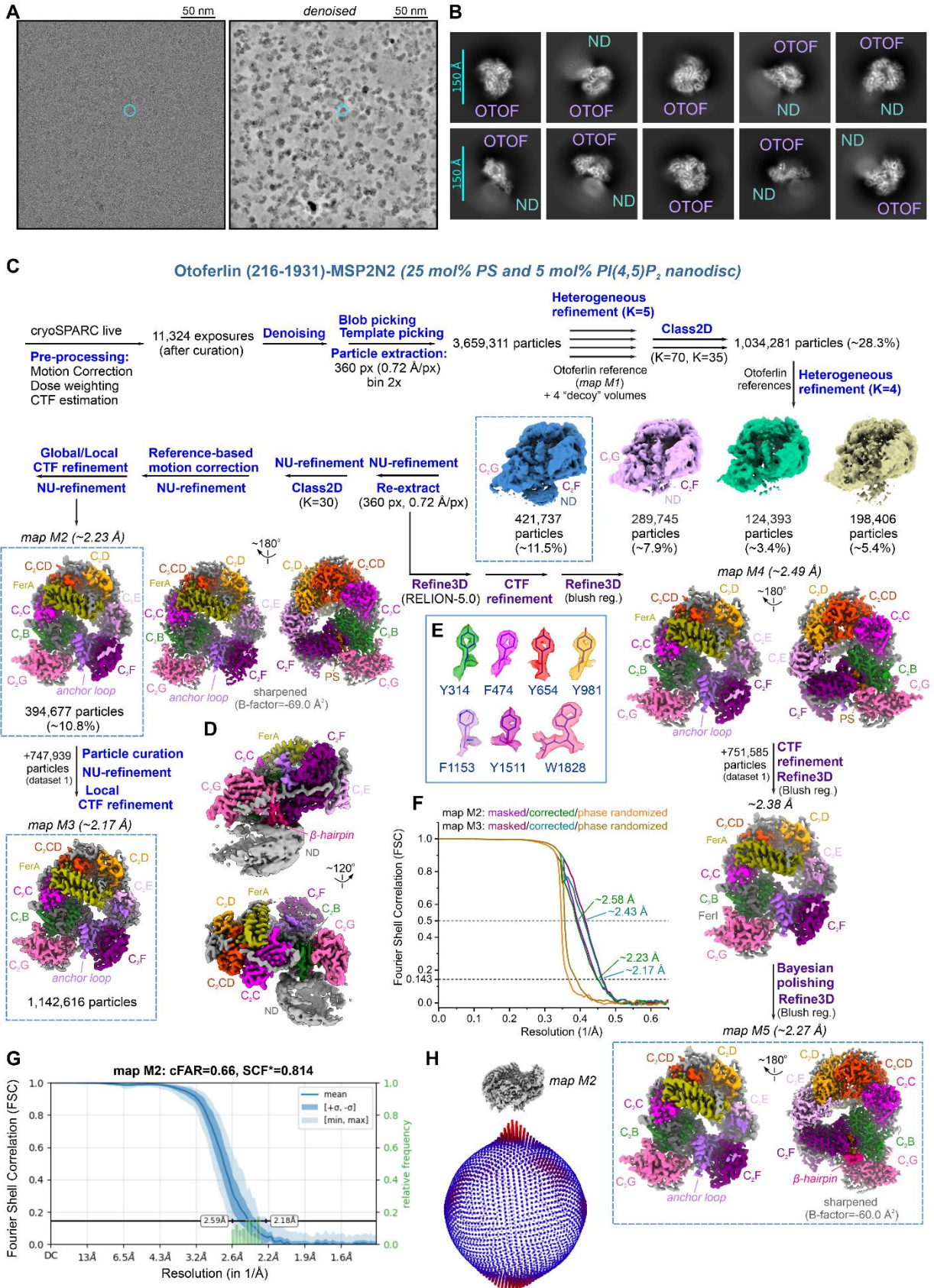


### **Figure S3. Cryo-EM analysis of the otoferlin (216-1931)-nanodisc complex**

#### **(25 mol% PS and 5 mol% PI(4,5)P<sub>2</sub> nanodisc)**

(A) Cryo-EM micrographs (raw and denoised) of the otoferlin (216-1931) bound to a 25 mol% DOPS and 5 mol% PI(4,5)P<sub>2</sub> MSP2N2 nanodisc. A lipid-bound otoferlin particle is circled for orientation purposes.

(B) 2D class averages of the otoferlin (216-1931)-nanodisc complex (25 mol% DOPS and 5 mol% PI(4,5)P<sub>2</sub> nanodisc). The density elements corresponding to otoferlin and the MSP2N2 nanodisc are indicated.

(C) Cryo-EM data processing schematic for the lipid-bound otoferlin (216-1931) complex, assembled on a nanodisc with 25 mol% DOPS and 5 mol% PI(4,5)P<sub>2</sub>. Processing steps shown in blue and purple were performed using cryoSPARC v.4.7 and RELION-5.0, respectively. The final maps used for model building are colour-coded by the resolved domains.

(D) Feature-enhanced map of the otoferlin (216-1931)-nanodisc complex. The locally scaled map was generated with LocScale and allows the better visualization of the low-resolution nanodisc density.

(E) Selected density snapshots from the high-resolution lipid-bound otoferlin (216-1931) cryo-EM map (map M9). The sharpened cryo-EM density map is contoured around several well-resolved otoferlin residues and coloured according to the otoferlin domain.

(F) Fourier shell correlation (FSC) plots between the cryo-EM half-maps of lipid-bound otoferlin (216-1931). The global resolution of the maps was estimated using the gold-standard FSC criterion (FSC=0.143).

(G) Fourier sampling and directional resolution of the lipid-bound otoferlin cryo-EM map (map M2). The sampling compensation factor (SCF) and the conical FSC area ratio (cFAR) were calculated using cryoSPARC v4.7.

(H) Angular distribution of the nanodisc-bound otoferlin (216-1931) particles used to reconstruct the map M2 of the complex. A higher number of particle images is indicated in red.



**Figure S4**

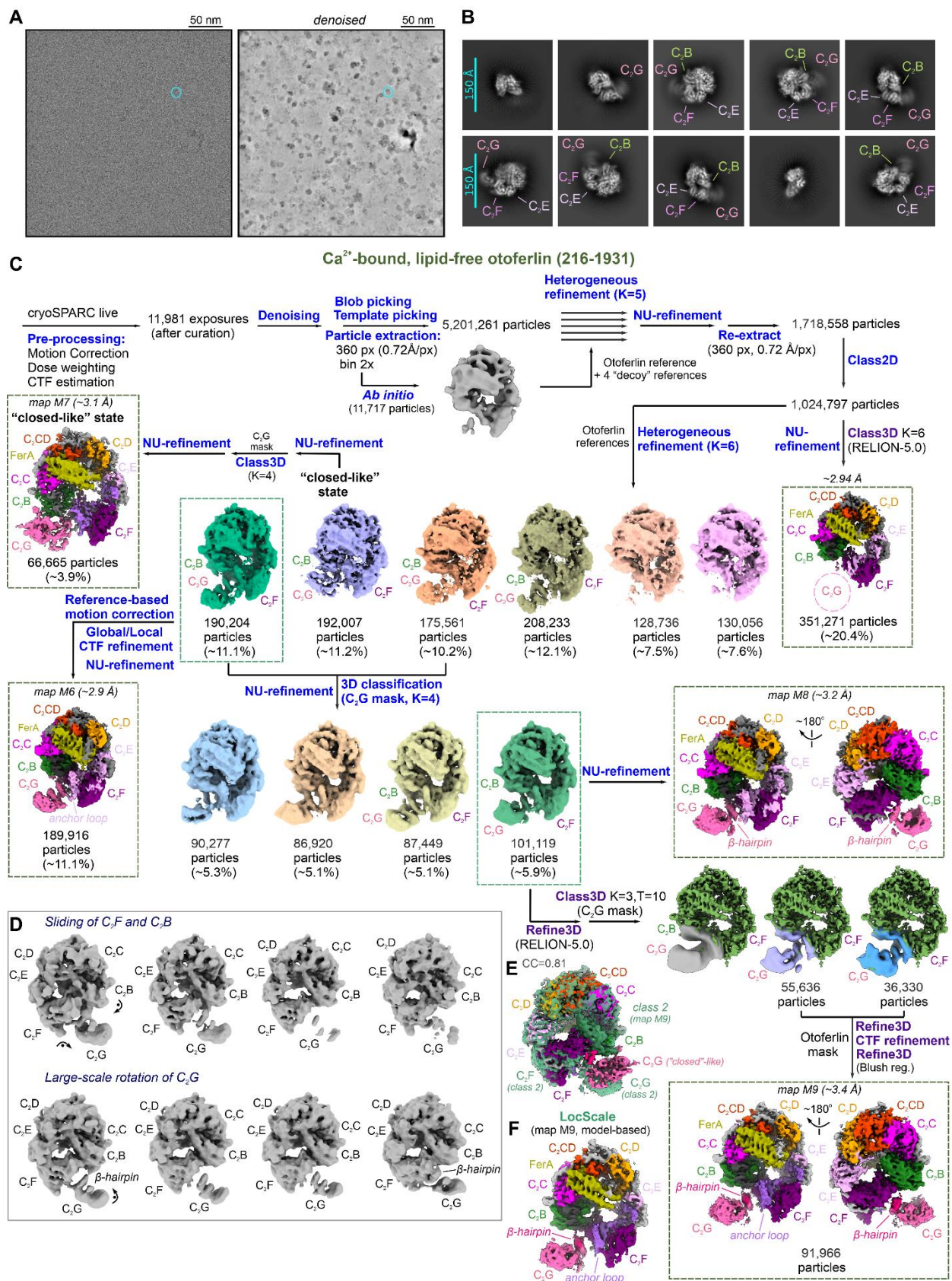




#### **Figure S4. Cryo-EM analysis of Ca<sup>2+</sup>-bound, lipid-free otoferlin (216-1931)**

(A) Denoised cryo-EM micrograph of lipid-free otoferlin (216-1931) imaged in vitreous ice. A typical otoferlin (216-1931) particle is circled in cyan.

(B) Reference-free 2D class averages of the lipid-free otoferlin (216-1931). Note that the C-terminal C<sub>2</sub>G domain is dynamic in the absence of a lipid bilayer (see also Fig. S2B).

(C) Cryo-EM processing schematic for the lipid-free otoferlin (216-1931). The resolution of the final maps was estimated using the FSC=0.143 criterion. The final lipid-free otoferlin (216-1931) maps were colored as in Figure S2C.

(D) Conformational dynamics of otoferlin (216-1931) in the lipid-free state. Selected map snapshots along the two resolved modes of 3D variability are shown side by side. Particle motions in the lipid-free state primarily involve the C<sub>2</sub>B, C<sub>2</sub>F, and the highly dynamic C<sub>2</sub>G domain.

(E) Superposition of the “open” and “closed”-like maps of Ca<sup>2+</sup>-bound, lipid-free otoferlin. The “closed”-like state map (map M7) is colour-coded by modelled domains, while the “open” state map (class 2, map M9) is shown in light green.

(F) Locally scaled map of Ca<sup>2+</sup>-bound, lipid-free otoferlin. The map (map M9, class 2) was scaled with LocScale using the refined structural model (model-based) to visualize the dynamic C<sub>2</sub>G domain.

**Figure S5**

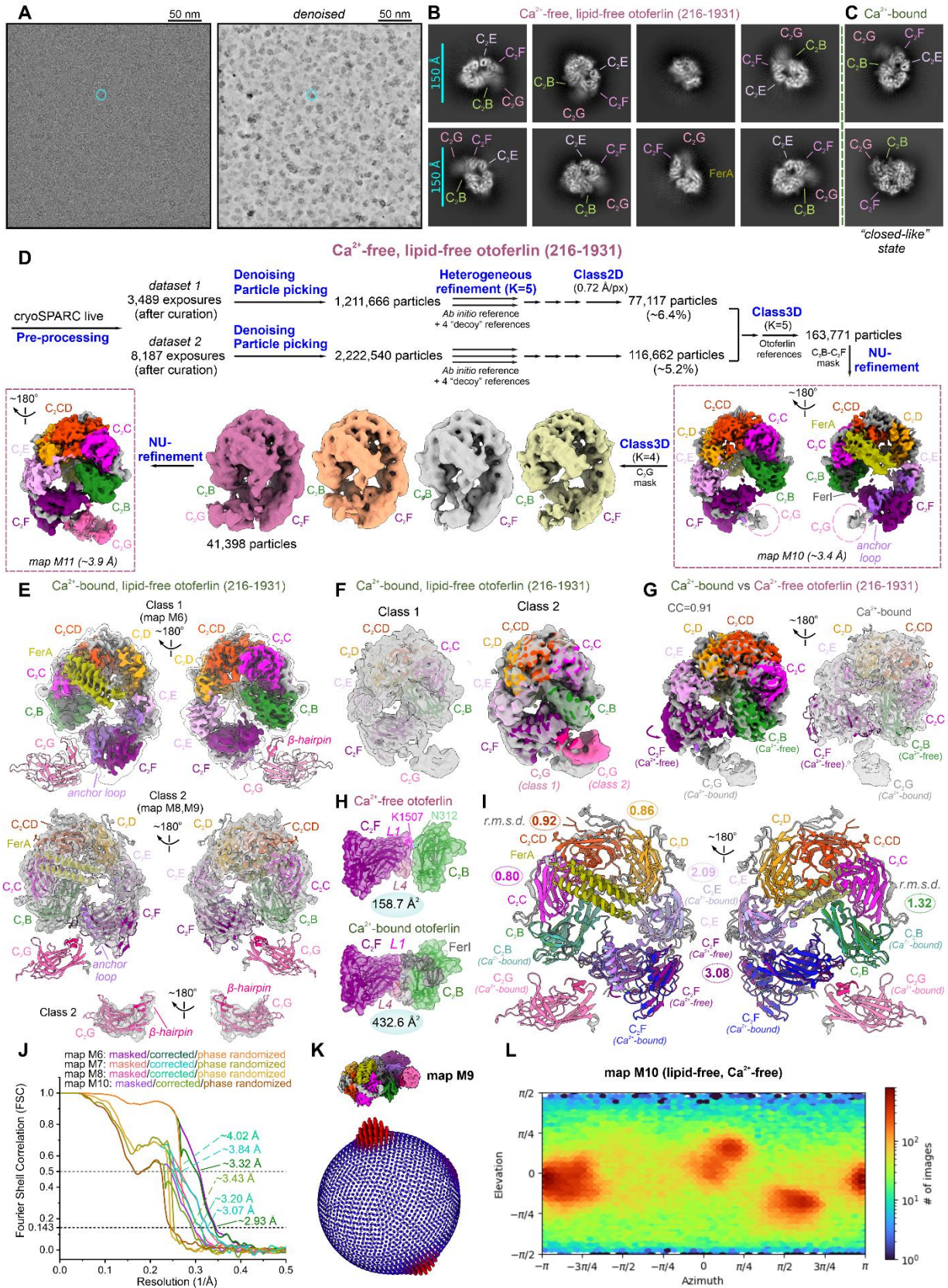


### Figure S5. Cryo-EM image analysis of $\text{Ca}^{2+}$ -free, lipid-free otoferlin (216-1931)

(A) Cryo-EM micrograph (raw and denoised) of vitrified otoferlin (residues 216-1931) in the  $\text{Ca}^{2+}$ -free, lipid-free state. A typical otoferlin particle is circled.

(B) Representative 2D class averages of otoferlin (216-1931) imaged in the absence of  $\text{Ca}^{2+}$  and lipids. The assigned otoferlin domains are indicated.

(C) 2D class averages of lipid-free otoferlin (216-1931) imaged in the presence of  $\text{Ca}^{2+}$  (see also Fig. S2B). These 2D averages are shown for comparison with the  $\text{Ca}^{2+}$ -free 2D classes in panel B; additional 2D averages are provided in Fig. S2B. Note the “closed”-like 2D classes observed in the presence of  $\text{Ca}^{2+}$ , which may indicate that  $\text{Ca}^{2+}$  ions stabilize the poses of the C<sub>2</sub>F and C<sub>2</sub>G domains (see also Fig. S4C and S4E).

(D) Cryo-EM image processing schematic for the  $\text{Ca}^{2+}$ -free otoferlin (216-1931). Key processing steps are indicated, and the final maps are coloured according to the modelled otoferlin domains.

(E) The two resolved 3D classes of  $\text{Ca}^{2+}$ -bound lipid-free otoferlin (216-1931). The two conformations of lipid-free otoferlin differ in the orientation of the C-terminal C<sub>2</sub>G domain and correspond to “open” otoferlin states. The final models were fitted into the refined cryo-EM maps and colour-coded. The flexible C<sub>2</sub>G domain was fitted into either a 6 Å (top panel) or 3.9 Å (bottom panel) low-pass filtered maps, which are shown as transparent surfaces.

(F) Comparison between the two resolved states of  $\text{Ca}^{2+}$ -bound, lipid-free otoferlin (216-1931). The two otoferlin maps were aligned and the similar C<sub>2</sub>B-C<sub>2</sub>F domains are shown as either model (left) or cryo-EM density maps (right).

(G) Comparison between the  $\text{Ca}^{2+}$ -free and  $\text{Ca}^{2+}$ -bound otoferlin (216-1931) maps in the lipid-free state. Note the different orientation of the C<sub>2</sub>F domain and the absence of density (or weak density in map M11, S5D) for the C<sub>2</sub>G domain in the  $\text{Ca}^{2+}$ -free state. Cryo-EM maps and models are depicted as in E-F.

(H) The C<sub>2</sub>B-C<sub>2</sub>F interface in the  $\text{Ca}^{2+}$ -free and  $\text{Ca}^{2+}$ -bound, lipid-free otoferlin. The C<sub>2</sub>B and C<sub>2</sub>F domains are shown as solvent-excluded surfaces, and interface areas are indicated (see also Fig. 4F).

(I) Structural superposition of  $\text{Ca}^{2+}$ -free and  $\text{Ca}^{2+}$ -bound, lipid-free otoferlin. The C<sub>2</sub>B and C<sub>2</sub>E-C<sub>2</sub>G domains are shown in different colours. Root-mean-square deviations (r.m.s.d.) of the domains' backbone ( $\text{C}\alpha$ ) between the two lipid-free conformations are indicated.

(J) Fourier shell correlation (FSC) plots for the lipid-free otoferlin (216-1931) cryo-EM maps. FSCs were calculated between cryo-EM half-maps and the resolution of the maps were estimated according to the gold-standard FSC criterion ( $\text{FSC}=0.143$ ).

(K-L) Angular distribution of the lipid-free otoferlin particles in the final  $\text{Ca}^{2+}$ -bound (map M9) and  $\text{Ca}^{2+}$ -free (map M10) cryo-EM maps. Higher particle numbers at given projection angles are indicated in red.



1



**Figure S6. Cryo-EM densities of otoferlin's core domains (C<sub>2</sub>B-C<sub>2</sub>D) in the lipid-bound state**

(A) Cryo-EM density of the C<sub>2</sub>B domain in the lipid-bound state of otoferlin (216-1931). The top loops of C<sub>2</sub>B (L1-L4) are colour-coded. Selected  $\beta$ -strand densities are contoured around the fitted model.

(B) The resolved C<sub>2</sub>A-C<sub>2</sub>B linker (residues 239-265) in the “closed”, lipid-bound state of otoferlin (216-1931). The modelled C<sub>2</sub>A-C<sub>2</sub>B linker (depicted as sticks with its cryo-EM density) engages the  $\alpha$ -helices of the FerA module at multiple sites before reaching the membrane-bound N-terminal C<sub>2</sub>B domain.

(C) Cryo-EM density of the FerI motif in otoferlin's lipid-bound state. The FerI motif (residues 396-428) connects the N-terminal C<sub>2</sub>B to the C<sub>2</sub>C domain; the fitted FerI model is shown with the cryo-EM density.

(D) Cryo-EM density of the Ca<sup>2+</sup>-bound C<sub>2</sub>C domain. The cryo-EM density (cyan) is contoured around the single bound Ca<sup>2+</sup> ion, and the top loops (L1-L4) are indicated. Several  $\beta$ -strands of C<sub>2</sub>C are shown with their cryo-EM densities.

(E) Structure of otoferlin's C<sub>2</sub>CD-FerA module. The C<sub>2</sub>CD-FerA region packs between the C<sub>2</sub>C and C<sub>2</sub>D domains. Cryo-EM densities of FerA's four-helix bundle and of selected  $\beta$ -strands from C<sub>2</sub>CD are shown with the final models.

(F) Cryo-EM density of otoferlin's C<sub>2</sub>D domain. C<sub>2</sub>D coordinates two Ca<sup>2+</sup> ions independently of phospholipid binding. Two representative  $\beta$ -strands are shown as stick models with their cryo-EM densities.

(G-H) The two Ca<sup>2+</sup>-binding sites of otoferlin's C<sub>2</sub>D domain. The Ca<sup>2+</sup>-coordinating residues of C<sub>2</sub>D (G) and the neighboring L4 loop of C<sub>2</sub>E (H) are shown as sticks with the contoured cryo-EM density.

(I) Cryo-EM densities of selected  $\beta$ -strands in the C<sub>2</sub>E domain. The  $\beta$ -strands are depicted as sticks, and the density is contoured around the C<sub>2</sub>E model.

**Figure S7**

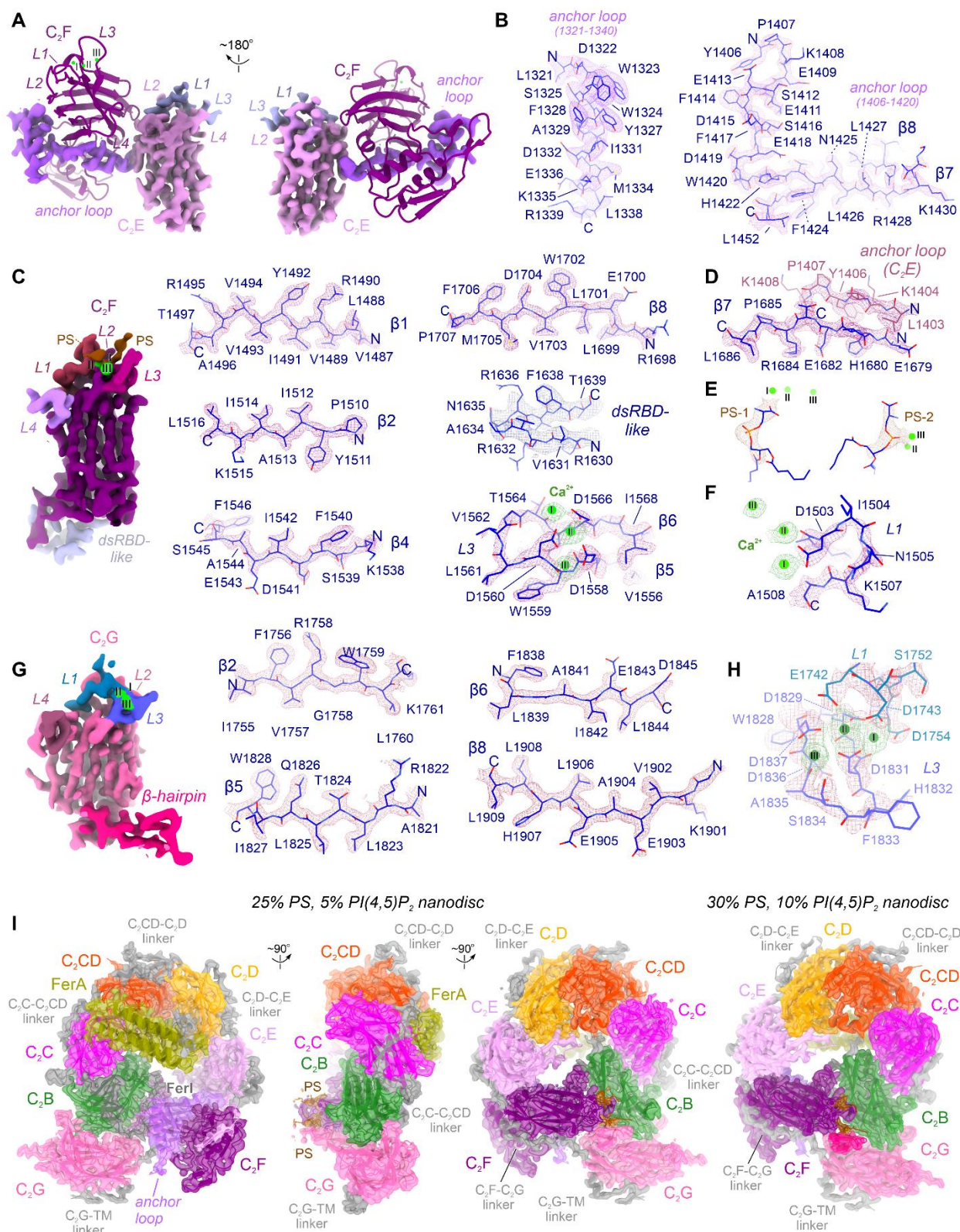


**Figure S7. Cryo-EM densities of otoferlin's C-terminal domains (C<sub>2</sub>E-C<sub>2</sub>G) in the lipid-bound state**

- (A) Cryo-EM density of the C<sub>2</sub>E domain. C<sub>2</sub>E links the otoferlin core (C<sub>2</sub>B-C<sub>2</sub>D) to the C-terminal C<sub>2</sub>F-C<sub>2</sub>G domains. C<sub>2</sub>E contains a large insertion loop (the “anchor loop”, residues 1238-1421) between the  $\beta$ 6 and  $\beta$ 7 strands, which is mostly unstructured and wraps around C<sub>2</sub>F (purple).
- (B) Cryo-EM densities of selected anchor loop elements in the lipid-bound state of otoferlin. Resolved regions include a helical element (residues 1321-1340) and several segments connecting the  $\beta$ 6- $\beta$ 7 strands (residues 1238-1265 and 1398-1421). Cryo-EM densities of these regions are shown with the corresponding models.
- (C) Structure of the C-terminal C<sub>2</sub>F domain in the lipid-bound state of otoferlin. Three bound Ca<sup>2+</sup> ions, two PS (phosphatidylserine) molecules, and the top loops (L1-L4) are indicated. Cryo-EM densities of selected  $\beta$ -strands and modelled Ca<sup>2+</sup> ions are contoured around the C<sub>2</sub>F model.
- (D) Contact interface between the C<sub>2</sub>E anchor loop and the  $\beta$ 7 strand of C<sub>2</sub>F. The modelled otoferlin elements are shown as sticks with contoured cryo-EM densities.
- (E) Cryo-EM densities of the two molecules PS molecules originating from the lipid nanodisc. The phospholipid headgroups are bound to C<sub>2</sub>F through three coordinated Ca<sup>2+</sup> ions, shown as spheres for orientation purposes.
- (F) The three Ca<sup>2+</sup>-binding sites of C<sub>2</sub>F. C<sub>2</sub>F coordinates three Ca<sup>2+</sup> ions via residues in the L1-L3 loops and two recruited PS molecules (E). The cryo-EM density is contoured around the modelled ions.
- (G) Cryo-EM density of the C-terminal C<sub>2</sub>G domain in the lipid-bound state of otoferlin. The modelled Ca<sup>2+</sup> ions, the top loops (L1-L4), and the  $\beta$ -hairpin motif of C<sub>2</sub>G are highlighted. Several  $\beta$ -strands are shown as cryo-EM densities.
- (H) The Ca<sup>2+</sup>-binding sites of otoferlin's C<sub>2</sub>G domain. As in C<sub>2</sub>F, the L1-L3 loops of C<sub>2</sub>G coordinate three Ca<sup>2+</sup> ions (shown as spheres with contoured densities). The Ca<sup>2+</sup> ions were likely coordinated independent of phospholipids, as no phospholipid headgroups could be modelled in the C<sub>2</sub>G cryo-EM map. The Ca<sup>2+</sup>-coordinating residues are shown as sticks.
- (I) Modelling of otoferlin (216-1931) in the lipid-bound state. Final cryo-EM maps of the two otoferlin-nanodisc complexes (map M1 and map M2), assembled on either 25 mol% PS and 5 mol% PI(4,5)P<sub>2</sub> or 30 mol% PS and 10 mol% PI(4,5)P<sub>2</sub> MSP2N2 nanodiscs, are coloured according to the modelled otoferlin domains. The final otoferlin models are shown inside the maps. Resolved linker regions connecting the C<sub>2</sub> domains are coloured grey.



**Figure S8**

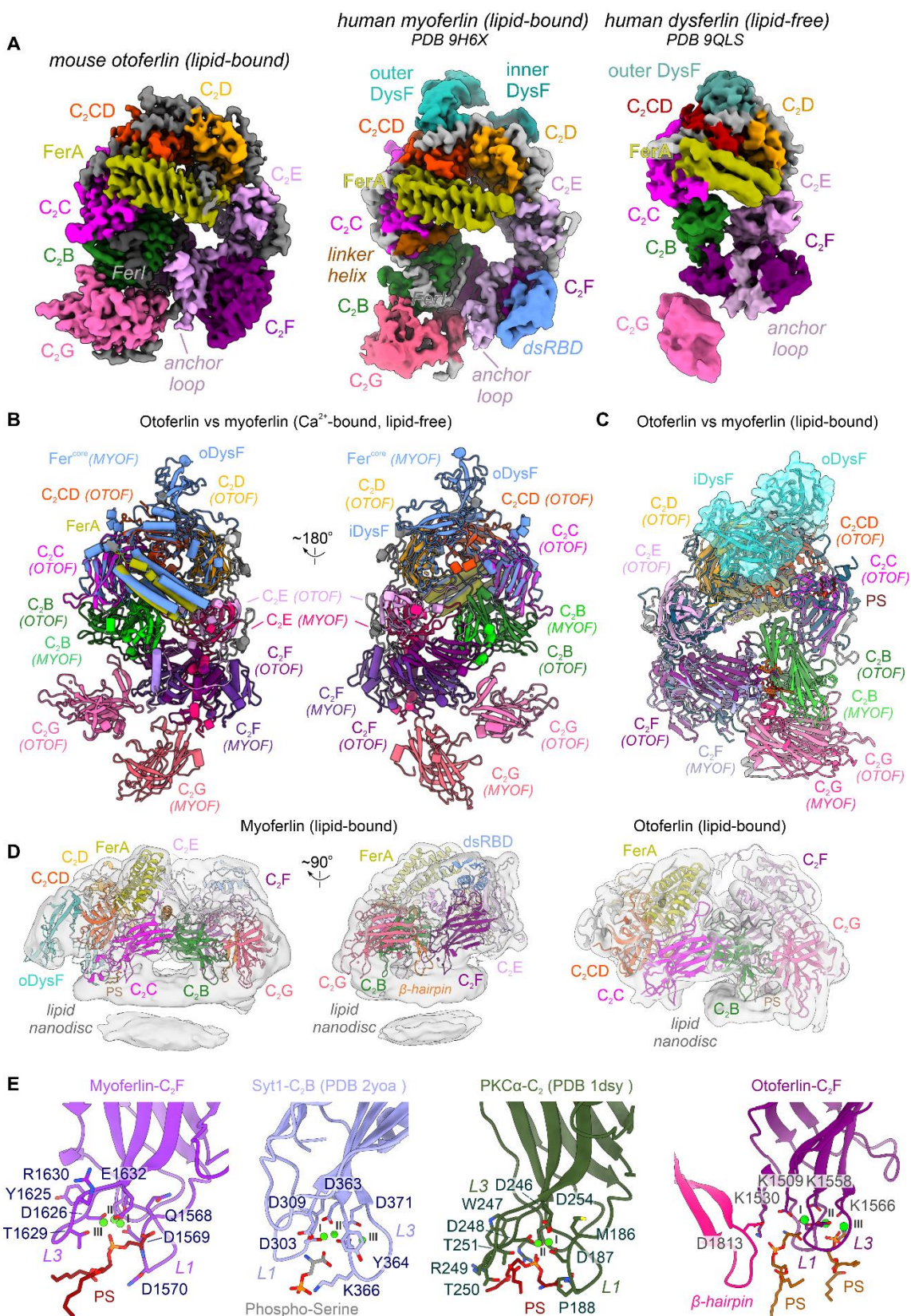




**Figure S8. Comparison between the cryo-EM structures of otoferlin, myoferlin, and dysferlin**

- (A) Side-by-side comparison between the cryo-EM structures of mouse otoferlin (lipid-bound state, residues 216-1931, this work), human myoferlin (lipid-bound state, residues 1-1997, PDB 9H6X), and human dysferlin ( $\text{Ca}^{2+}$ -bound, lipid-free state, residues 1-2017, PDB 9QLS). The cryo-EM maps are coloured after the modelled domains and are viewed from the solvent-facing side.
- (B) Structural superposition of mouse otoferlin (216-1931) and human myoferlin (1-1997, 9QLN) in their  $\text{Ca}^{2+}$ -bound, lipid-free states. While the ferlin core domains ( $\text{C}_2\text{C}$ - $\text{C}_2\text{CD}$ -FerA- $\text{C}_2\text{D}$ ) have a similar organization, the two structures differ in the positions of the N-terminal  $\text{C}_2\text{B}$  and the  $\text{C}_2\text{E}$ - $\text{C}_2\text{G}$  domains.  $\text{C}_2\text{B}$  and  $\text{C}_2\text{E}$ - $\text{C}_2\text{G}$  are highlighted in different colours. Note that the DysF motifs, the outer DysF (oDysF) and the inner DysF (iDysF), are absent in otoferlin.
- (C) Superposition of lipid-bound mouse otoferlin (216-1931) and human myoferlin (1-1997, PDB 9H6X/PDB 9QLF). The structures were aligned based on the ferlin core domains ( $\text{C}_2\text{C}$ - $\text{C}_2\text{D}$ ). The  $\text{C}_2\text{B}$  and  $\text{C}_2\text{E}$ - $\text{C}_2\text{G}$  domains adopt comparable orientations and the overall configuration of the ferlin ring is highly similar.
- (D) Protein-lipid interfaces in the nanodisc-bound structures of human myoferlin (1-1997, PDB 9H6X) and mouse otoferlin (216-1931, this work). The ferlin models are colour-coded and fitted into 8 Å (myoferlin) or 6 Å (otoferlin) low-pass filtered maps of the nanodisc-bound complexes. In both structures, the  $\text{C}_2\text{B}$  and  $\text{C}_2\text{F}$ - $\text{C}_2\text{G}$  domains interact with the lipid nanodisc. However, the  $\text{C}_2\text{C}$  domain and the iDysF motif (absent from otoferlin) provide additional contacts in the myoferlin structure.
- (E)  $\text{Ca}^{2+}$ -sensitive recognition of phosphatidylserine (PS) headgroups in otoferlin, myoferlin, and in other  $\text{C}_2$  domain structures. The  $\text{C}_2$  domain models are shown in cartoon representation, with bound  $\text{Ca}^{2+}$  ions depicted as spheres. Aided by the  $\beta$ -hairpin motif of  $\text{C}_2\text{G}$ , the  $\text{C}_2\text{F}$  domain of otoferlin recognizes two PS molecules via three coordinated  $\text{Ca}^{2+}$  ions, compared with a single PS headgroup in myoferlin's  $\text{C}_2\text{F}$  (PDB 9H6X), synaptotagmin-1 (Syt1)  $\text{C}_2\text{B}$  (PDB 2yoa), or the  $\text{C}_2$  domain of PKC $\alpha$  (PDB 1dsy).

**Figure S9**

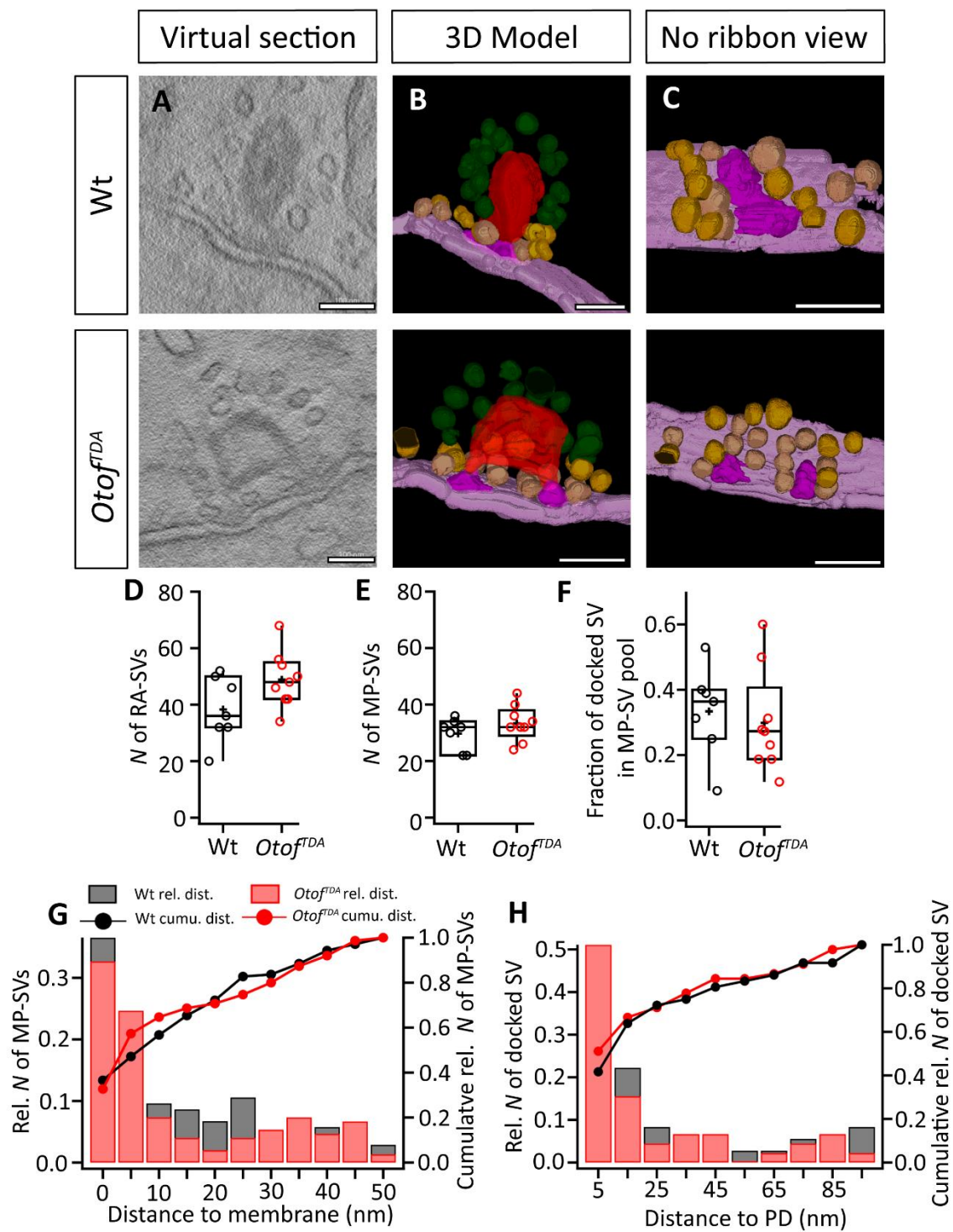


**Figure S9. Disruption of  $\text{Ca}^{2+}$ -binding by the C2F domain (previously C2E domain) does not change SV number and distribution at ribbon synapses**

(A) Representative virtual electron tomogram sections of IHC ribbon synapses from an *Otof*<sup>D1563/1565/1570A</sup> (*Otof*<sup>ADA</sup>) animal and an *Otof*<sup>wt</sup> (here abbreviated Wt) control. Scale bar: 100 nm.

(B) Reconstructed model of the area around the ribbon synapses for the tomograms corresponding to sections from A. The ribbon is rendered in red, the presynaptic density in magenta, and the active zone membrane in soft pink. Vesicles are classified into three pools, ribbon-associated (RA-SV, green), membrane-proximal (MP-SV, orange), and docked (pink). Scale bar: 100 nm.

(C) Top view onto the AZ reconstructions with MP-SVs, ribbon and RA-SVs are not displayed in this perspective. Scale bar: 100 nm.

(D) Number (*N*) of RA-SVs per ribbon synapse. The numbers were not significantly different in IHCs of *Otof*<sup>ADA</sup> animals compared to Wt ( $N_{wt} = 19.1 \pm 2.2$ ,  $n = 7$  ribbons,  $N_{animals} = 1$  vs.  $N_{mut} = 24.4 \pm 1.6$ ,  $n = 9$  ribbons,  $N_{animals} = 2$ , Wilcoxon signed-rank test:  $p > 0.05$ ).

(E) Number (*N*) of MP-SVs per ribbon synapse. The numbers were not significantly different in IHCs of *Otof*<sup>ADA</sup> animals compared to Wt ( $N_{wt} = 14.9 \pm 1.1$ ,  $n = 7$  ribbons vs.  $N_{mut} = 16.7 \pm 1.0$ ,  $n = 9$  ribbons, Wilcoxon signed-rank test:  $p > 0.05$ ).

(F) Fraction of docked SVs in the MP-SV pool per ribbon synapse. The fractions were not significantly different in IHCs of *Otof*<sup>ADA</sup> animals compared to Wt ( $Fraction_{wt} = 0.334 \pm 0.051$ ,  $n = 7$  ribbons vs.  $Fraction_{mut} = 0.298 \pm 0.052$ ,  $n = 9$  ribbons, Wilcoxon signed-rank test:  $p > 0.05$ ).

(G) Distance of MP-SVs to the active zone membrane, histogram with bins of 3.3 nm for wt (gray) and KO (red) and cumulative distribution (Wt: black, *Otof*<sup>ADA</sup>: red). The distances were not significantly different in IHCs of *Otof*<sup>ADA</sup> animals compared to Wt ( $distance_{wt} = 13.8 \pm 1.4$  nm,  $n = 104$  MP-SVs vs.  $distance_{mut} = 13.8 \pm 1.3$  nm,  $n = 150$  MP-SVs, Wilcoxon signed-rank test:  $p > 0.05$ ).

(H) Distance of docked SVs to the presynaptic density. It was not significantly different in IHCs of *Otof*<sup>ADA</sup> animals compared to Wt ( $distance_{wt} = 25.4 \pm 5.0$  nm,  $n = 36$  docked SVs vs.  $distance_{mut} = 22.7 \pm 4.3$  nm,  $n = 45$  ribbons, Wilcoxon signed-rank test:  $p > 0.05$ ).

For further information see Table S4.

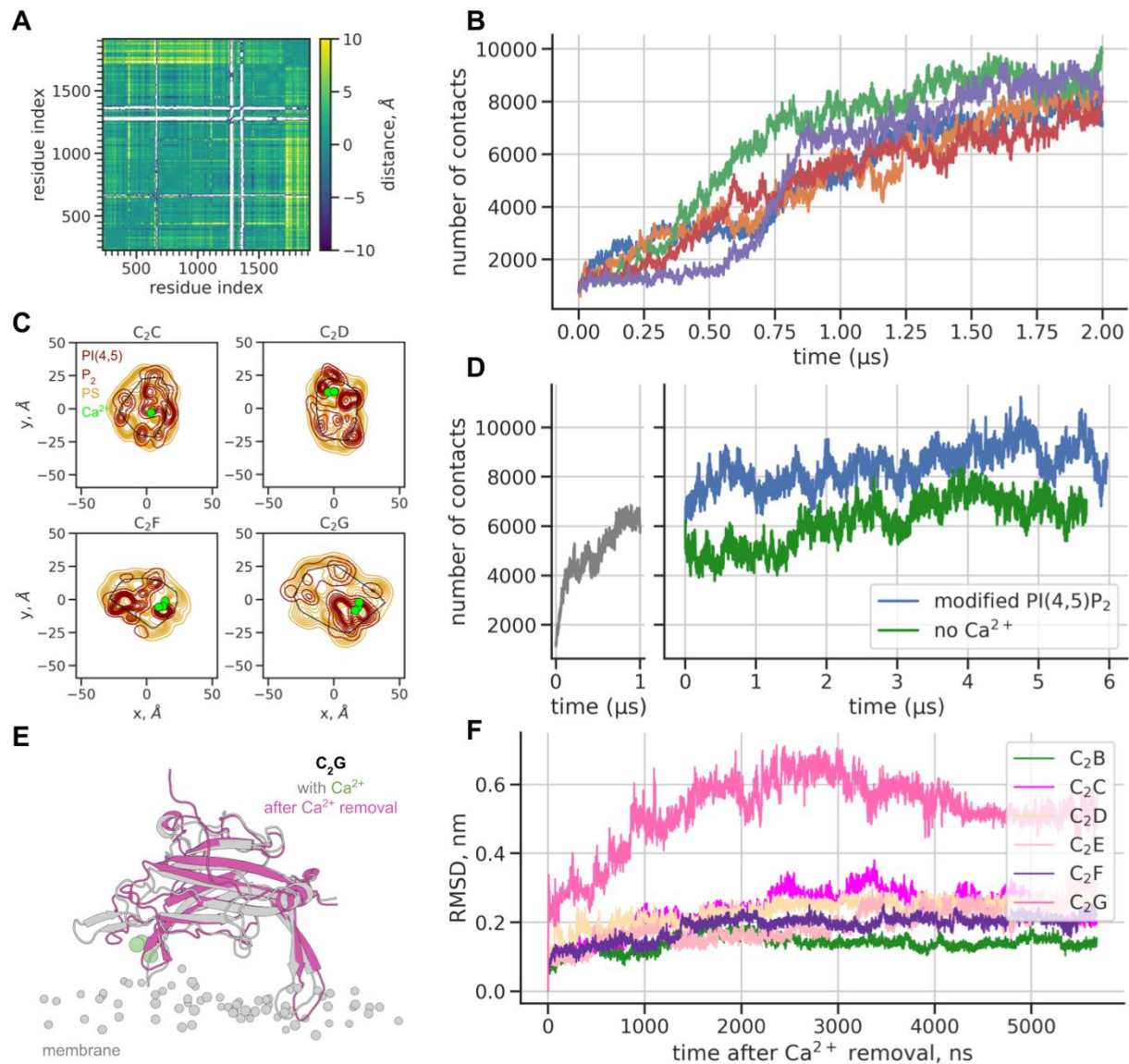


**Figure S10. MD simulations provide evidence that electrostatic interactions contribute to the otoferlin lipid binding, but are not the only source of protein-membrane interaction.**

(A) Differences between the performed MD simulations and the cryo-EM structure. The matrix shows, color coded, the difference between the average C<sub>α</sub> contact matrix calculated for the last 200 ns of the five simulation replicates and the C<sub>α</sub> contact matrix calculated for the initial cryo-EM structure. For visualization purposes, all the values below -10 Å or above 10 Å, corresponding to disordered regions of the protein, were masked out.

(B) Increased binding interface. Shown are the time traces of the number of interatomic contacts between otoferlin and membrane in five simulation replicates which started from the cryo-EM structure of lipid-bound otoferlin.

(C) Kernel density estimates for PS (yellow) and PI(4,5)P<sub>2</sub> (in red) together with contours of calcium-binding C<sub>2</sub> domains projected onto the membrane plane. Positions of calcium ions are



indicated by green dots. The origin of the plots is located at the projection of the center of mass of every C<sub>2</sub> domain. Densities were scaled by the number of observations for the lipid type separately for every C<sub>2</sub> domain.

(D) Lipid interface of otoferlin during initial binding (starting from an MD-equilibrated structure with a modelled transmembrane domain which was removed prior to system assembly for the simulation run) and in two experimental conditions in MD simulations. The last frame of the simulation of initial binding was used as the starting point for both conditions.

(E) Conformations of the C<sub>2</sub>G domain before (gray) and after (magenta) Ca<sup>2+</sup> removal in the simulations described in D. Coordinates were aligned using only the C<sub>α</sub> atoms of the C<sub>2</sub>G domain. The three calcium ions bound to C<sub>2</sub>G before simulations are indicated in green. The phosphorus atoms of lipid headgroups before Ca<sup>2+</sup> removal are depicted as spheres. After Ca<sup>2+</sup> removal, C<sub>2</sub>G partly detached from the lipid membrane, which is not displayed for clarity of visualization.

(F) Root mean square deviation (RMSD) traces of C<sub>2</sub> domains after Ca<sup>2+</sup> removal. Domains were aligned to their starting conformations using the C<sub>α</sub> atoms, and the RMSDs of C<sub>α</sub> atoms were plotted over simulation time.

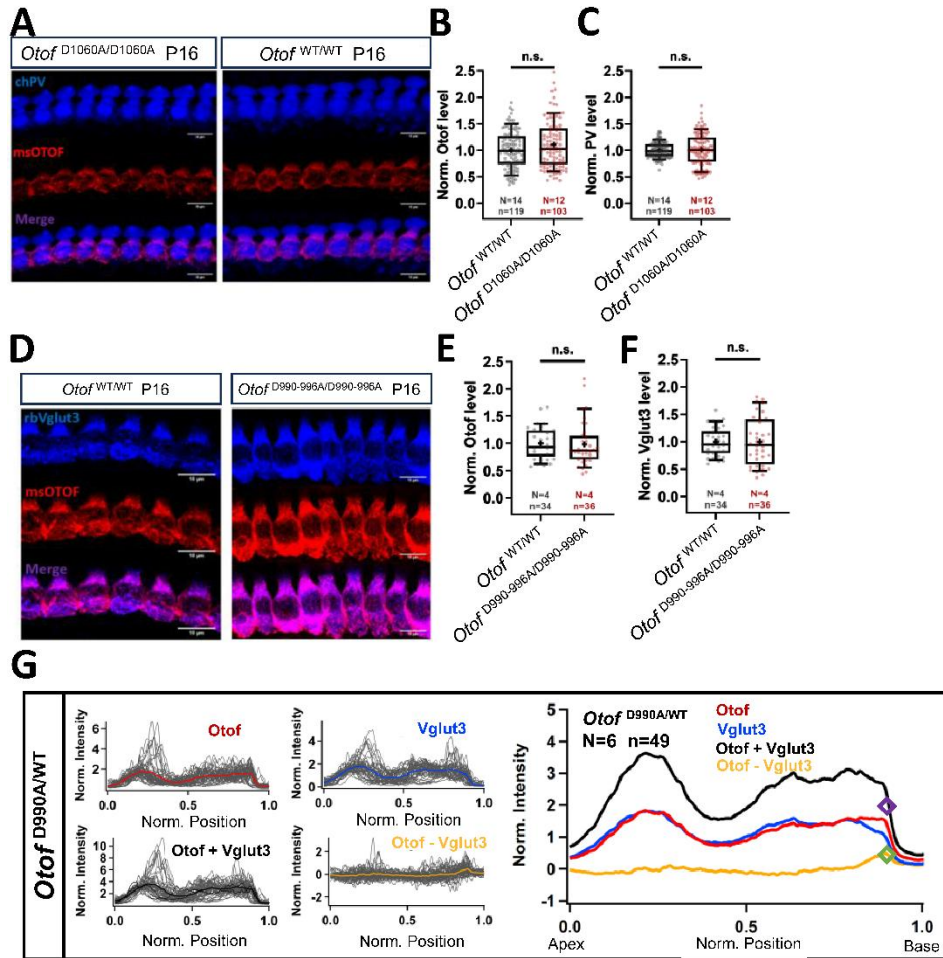


**Figure S11. Substantial expression and normal subcellular distribution of otoferlin in otoferlin mutant mice**

(A, D) Staining IHCs with otoferlin (OTOF) and parvalbumin (PV) / Vglut3 antibodies. Scale bar, 10  $\mu$ m.

(B, E) Otoferlin immunofluorescence intensity indicated unchanged otoferlin levels in *Otof*<sup>D1060A</sup> and *Otof*<sup>D990-996A</sup> IHCs compared to littermate control IHCs (Wilcoxon signed-rank test). Box and whisker plots represent median, 25th and 75th as well as 10th and 90th percentiles.

(C, F) Parvalbumin (PV) / Vglut3 immunofluorescence intensity indicated unchanged parvalbumin / Vglut3 levels in otoferlin mutant IHCs compared to littermate control IHCs (Wilcoxon signed-rank test). Box and whisker plots represent median, 25th and 75th as well as 10th and 90th percentiles.

(G) Line profile analysis. The line is indicated as a white dashed line in Fig.7A. The 0 and 1 indicate the start and end point of the line for line scans. For quantification of membrane staining, the fluorescence was normalized to the cellular fluorescence for each fluorophore. The sum of both

fluorescence values (black line) was used to determine the position of the basal membrane. At the most basal cellular point along this line which exceeds the threshold value of 2 (purple diamond), the otoferlin-Vglut3 fluorescence difference (yellow line) gave the value for relative otoferlin plasma membrane levels (green diamond).

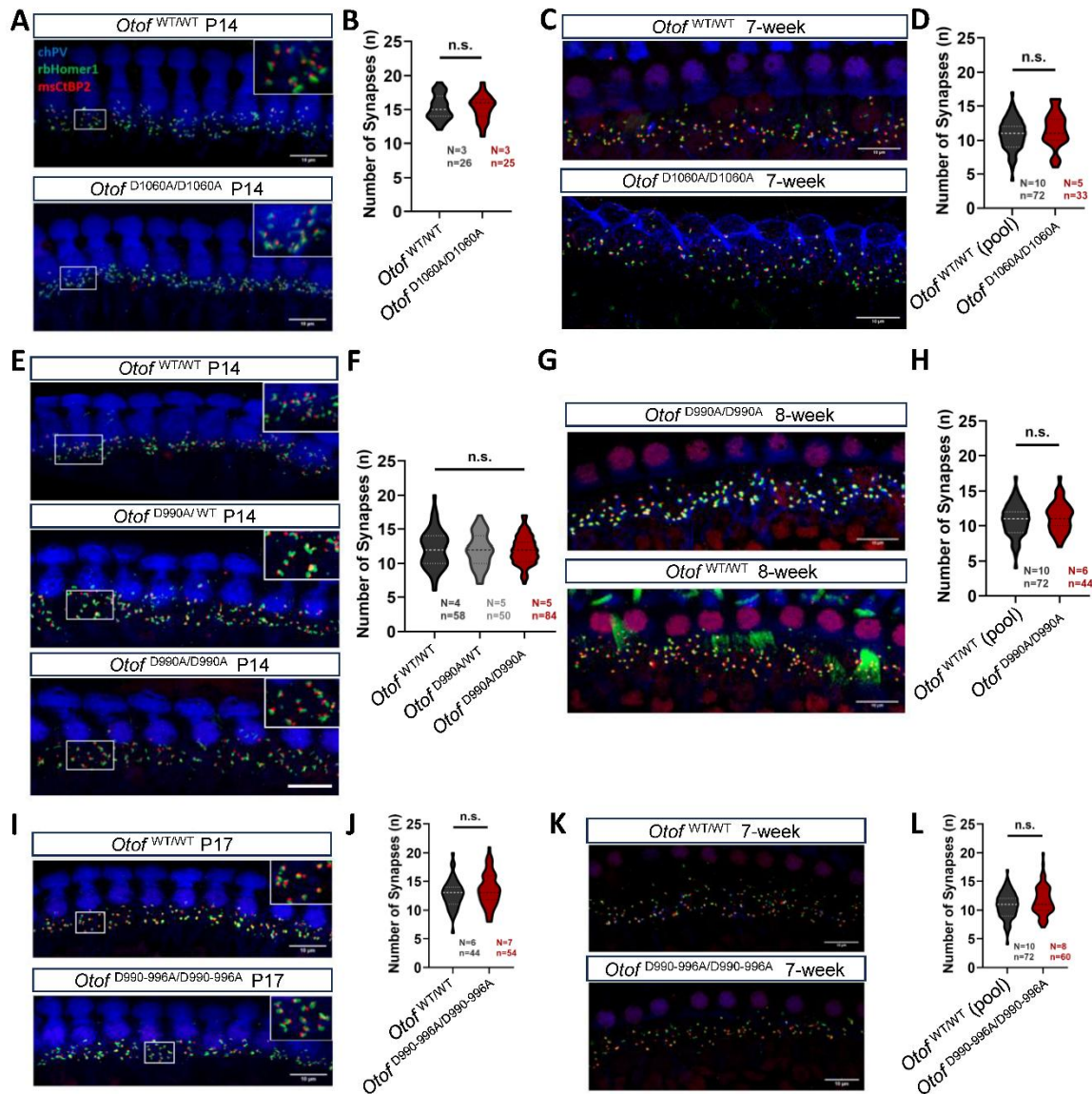


**Figure S12. The number of ribbon synapses in otoferlin mutant IHCs remain unchanged**

(A, E, I) Maximum-intensity projections of confocal stacks of P 2-week mouse IHCs of different genotypes following immunolabeling for parvalbumin (blue), ribeye (red) and homer-1 (green). Only juxtaposed red and green dots are counted as ribbon synapses. Scale bar, 10  $\mu$ m.

(B, F, J) Statistics showed that the numbers of ribbon synapses per IHC are similar between otoferlin mutant mice and littermate control mice at 2 weeks of age.

(C, G, K) Maximum-intensity projections of confocal stacks of P 8-week mouse IHCs of different genotypes following immunolabeling for parvalbumin (blue), ribeye (red) and homer-1 (green). Only juxtaposed red and green pairs are counted as ribbon synapses. Scale bar, 10  $\mu$ m.

(D, H, L) The numbers of ribbon synapses per IHC are similar between otoferlin mutant mice and littermate control mice at 8 weeks of age.



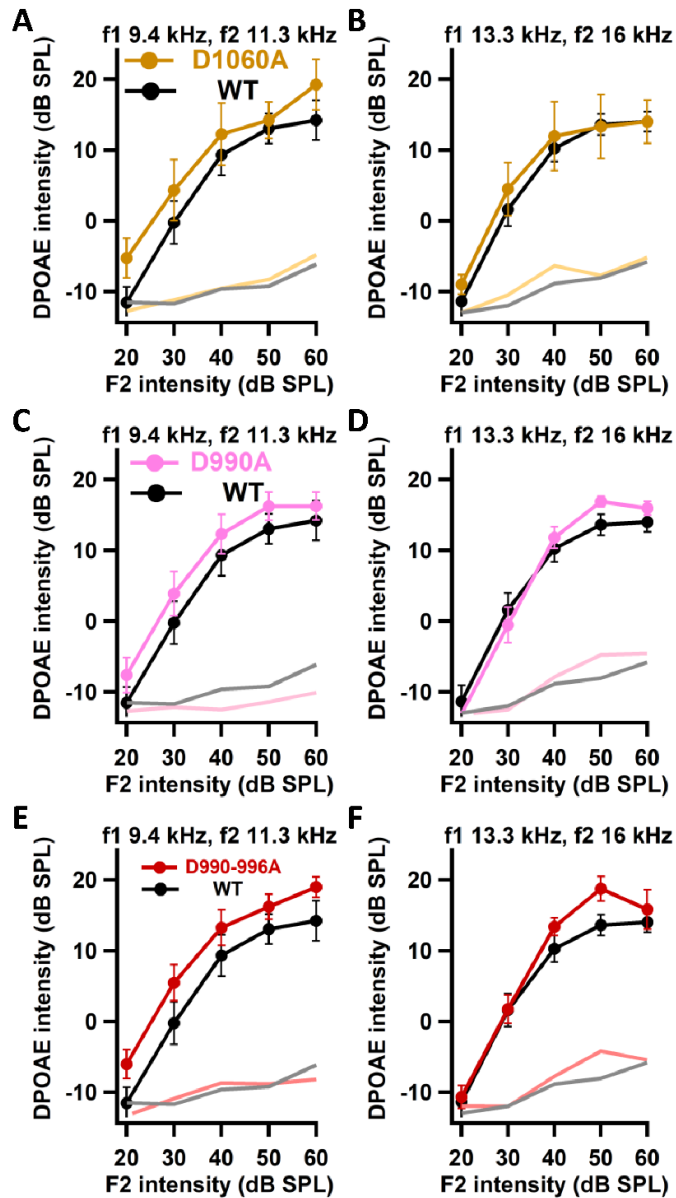


**Figure S13. Otoacoustic emissions indicate intact outer hair cell mediated cochlear amplification**

(A-B) Robust DPOAE in homozygous *Otof*<sup>D1060A</sup> mice (yellow, n=7) indicate normal OHC function across the cochlear frequency range. DPOAE growth function for two different pairs of stimulating primary tones: 9.4/11.3 kHz (A) and 13.3/16kHz (B).

C-D) Similarly, homozygous *Otof*<sup>D990A</sup> mice (magenta, n=8) and homozygous *Otof*<sup>D990-996A</sup> mice (E-F, red, n=9) have normal DPOAE across all tested frequency/intensity combinations. Data from the same 8 wildtype controls are shown in all panels in black. All data are displayed as mean±SEM. Light yellow/pink/grey lines indicate the average noise floor. No significant differences between mutant and wildtype mice were detected.

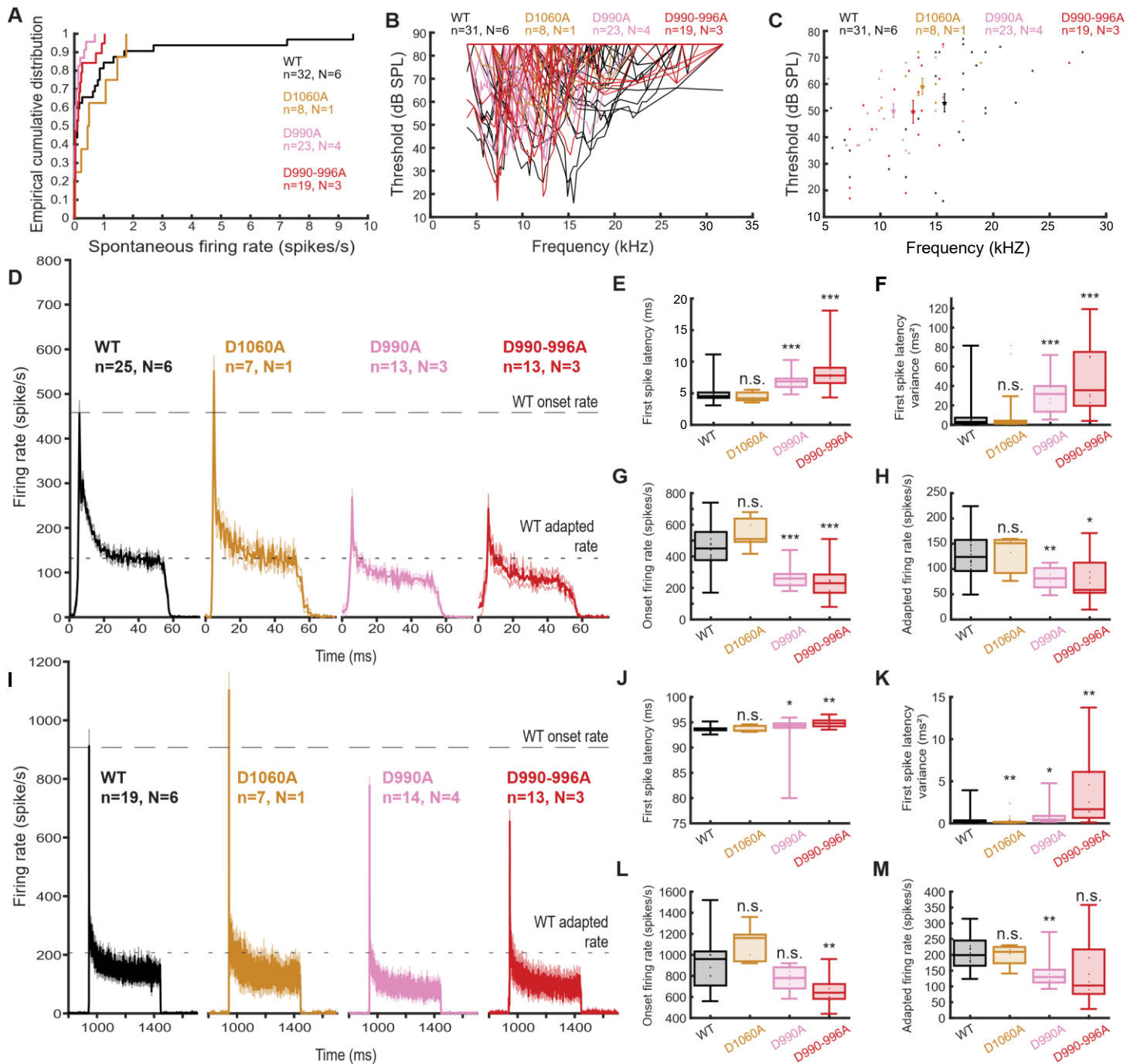


**Figure S14. Spontaneous and sound-evoked firing of spiral ganglion neurons indicate a reduced rate of initial release but largely intact vesicle replenishment at the afferent synapse of C2D mutants**

(A) Spontaneous firing rates of SGNs for *Otof*<sup>wt</sup> (black, N = 6, n = 32), homozygous *Otof*<sup>D1060A</sup> (yellow N = 1, n = 8), *Otof*<sup>D990A</sup> (magenta, N = 4, n = 24), and *Otof*<sup>D990-996A</sup> (red, N = 3, n = 19) mice displayed as an empirical cumulative distribution function.

(B) Tuning curves of SGNs for *Otof*<sup>wt</sup> (black, N = 6, n = 31), homozygous *Otof*<sup>D1060A</sup> (yellow N = 1, n = 8), *Otof*<sup>D990A</sup> (magenta, N = 4, n = 23), and *Otof*<sup>D990-996A</sup> (red, N = 3, n = 19) mice showing the sound pressure level (dB) at which a response above spontaneous firing rate was elicited for tone bursts of varying frequencies.

(C) Thresholds and characteristic frequencies of the SGNs from the tuning curves in b. Characteristic frequency was defined as the pure tone frequency that elicited a response above spontaneous firing at the lowest sound pressure level (dB). Means thresholds are indicated with stars and error bars represent the standard error of the mean (SEM).

(D) Peristimulus time histograms of SGN firing in response to 50 ms tonebursts at characteristic frequency and 30 dB above threshold with an 100ms interstimulus interval for *Otof*<sup>wt</sup> (black, N = 6, n = 25), homozygous *Otof*<sup>D1060A</sup> (yellow N = 1, n = 7), *Otof*<sup>D990A</sup> (magenta, N = 3, n = 13), and *Otof*<sup>D990-996A</sup> (red, N = 3, n = 13) mice. Mean traces are plotted with SEM indicated by fainter lines.

(E) Median first spike latency, (F) first spike latency variance, (G) onset firing rate, and (H) adapted firing rate of the SGNs shown in d.

(I) Peristimulus time histograms of SGN firing in response to 50 ms tonebursts at characteristic frequency and 30 dB above threshold with an 2000ms interstimulus interval for *Otof*<sup>wt</sup> (black, N = 6, n = 19), homozygous *Otof*<sup>D1060A</sup> (yellow N = 1, n = 7), *Otof*<sup>D990A</sup> (magenta, N = 4, n = 14), and *Otof*<sup>D990-996A</sup> (red, N = 3, n = 13) mice. Mean traces are plotted with standard error of the mean indicated by fainter lines.

(J) Median first spike latency, (K) first spike latency variance, (L) onset firing rate, and (M) adapted firing rate of the SGNs shown in d. One variance in first spike latency data point was excluded from the *Otof*<sup>D990A</sup> set (k) because it was more than 700 IQRs beyond the 3<sup>rd</sup> quartile. The removal of this data point did not affect the significance level of the statistical analyses. The unit from which this value was recorded was not removed from the dataset as other parameters we recorded were within acceptable ranges.

Data in E-H, and J-M, and P-R are shown as box and whisker plots with data points overlaid, median, 25th and 75th percentiles (box), 10th and 90th percentiles (whiskers) displayed.

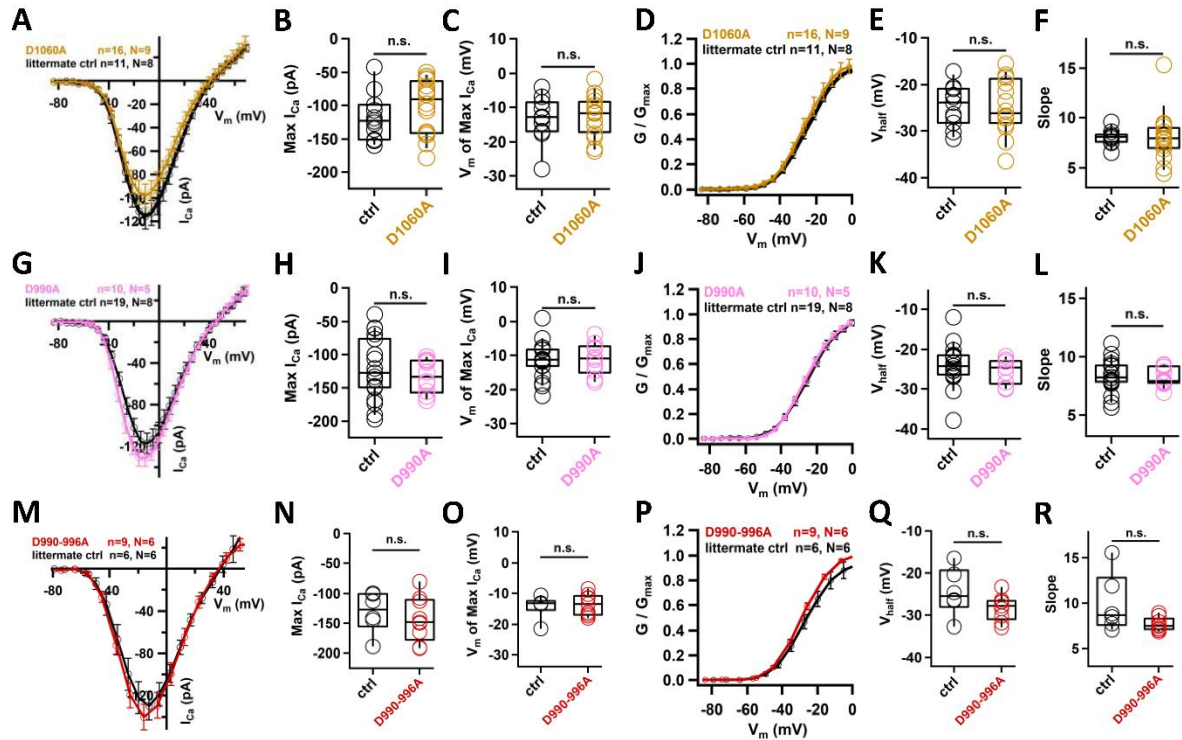


**Figure S15. Unchanged amplitude and voltage-dependence of activation of  $Ca^{2+}$ -influx in mutant IHCs**

(A-C, G-I, M-O) Current-voltage relationships of voltage-dependent  $Ca^{2+}$  currents (A, G, M) do not show significant differences in current amplitude (B, H, N) or voltage-dependence (C, I, O).

(D-F, J-L, P-R) Fractional activation of  $Ca^{2+}$  channels (D, J, P) extracted from the current-voltage relationships does not show significant difference in the voltage of half-maximal activation ( $V_{half}$ , E, K, Q) or voltage-sensitivity (slope, F, L, R).



**Table S1. Data collection, refinement and validation statistics for the otoferlin (216-1931)-nanodisc complexes**

	Map M1 (30% PS, 10% PI(4,5)P <sub>2</sub> ) PDB 9QE2, EMD-53046	Map M2 (25% PS, 5% PI(4,5)P <sub>2</sub> ) PDB 9SEA, EMD-54805	Map M5 (merged datasets) PDB 9SFL, EMD-54827
<b>Data collection and processing</b>			
Electron gun	X-FEG	X-FEG	
Detector	Falcon4i	Falcon4i	
Magnification	165,000	165,000	
Energy filter slit width (eV)	10	10	
Voltage (kV)	300.0	300.0	
Dose rate (e <sup>-</sup> /Å <sup>2</sup> /s)	15.2	15.8	
Electron exposure on sample (e <sup>-</sup> /Å <sup>2</sup> )	37.85	38.08	
Target defocus range (μm)	1.1-2.3	0.8-2.0	
Calibrated pixel size (Å)	0.72	0.72	
Symmetry imposed	C1	C1	
Collected movies (no.)	12,448	11,324	
Initial particle images (no.)	3,390,520	3,659,311	
Final particle images (no.)	751,004	394,677	
Map resolution at FSC=0.143 (Å)	2.3	2.23	
<b>Refinement</b>			
Initial model used	AlphaFold3	otoferlin (216-1931)	otoferlin (216-1931)
Model resolution (Å)	2.5	2.3	2.3
Model resolution at FSC=0.5 (Å)	2.53	2.43	2.32
Map sharpening B factor (Å <sup>2</sup> )	-85.7	-69.0	-60.0
<b>Model composition</b>			
Non-hydrogen atoms	12,479	12,380	12,381
Protein residues	1,547	1,533	1,533
Ligands	2x PS	2x PS	2x PS
Waters	-	-	1
Ions	9x Ca <sup>2+</sup>	9x Ca <sup>2+</sup>	9x Ca <sup>2+</sup>
<b>B factors (Å<sup>2</sup>)</b>			
Protein (min/max/mean)	52.28/210.98/103.85	57.65/195.91/102.11	35.99/204.73/83.36
Ligand (min/max/mean)	71.89/142.79/100.18	79.82/138.83/107.02	56.33/130.25/92.17
Water	-	-	55.54/55.54/55.54
<b>R.m.s. deviations</b>			
Bond lengths (Å)	0.005	0.004	0.005
Bond angles (°)	0.823	0.795	0.806
<b>Validation</b>			
Molprobity score	1.04	1.12	1.01
Clashscore	1.70	1.75	1.47
Rotamer outliers (%)	0.59	0.81	0.66
Cβ outliers (%)	-	-	-
CaBLAM outliers (%)	1.77	1.52	1.52
<b>Ramachandran plot</b>			
Favored (%)	97.4	96.91	97.37
Allowed (%)	2.54	2.96	2.56
Disallowed (%)	0.07	0.13	0.07

**Table S2. Data collection, refinement and validation statistics for the lipid-free otoferlin (216-1931) structures**

	Map M6 (class 1) Ca <sup>2+</sup> -bound PDB 9SEG, EMD-54809	Map M7 ("closed"-like) Ca <sup>2+</sup> -bound	Map M9 (class 2) Ca <sup>2+</sup> -bound PDB 9SE5, EMD-54802	Map M10 Ca <sup>2+</sup> -free PDB 9SH0, EMD-54883
<b>Data collection and processing</b>				
Electron gun	X-FEG			X-FEG
Detector	Falcon4i			Falcon4i
Magnification	165,000			165,000
Energy filter slit width (eV)	10			10
Voltage (kV)	300.0			300.0
Dose rate (e <sup>-</sup> /Å <sup>2</sup> /s)	15.5			15.03
Electron exposure on sample (e <sup>-</sup> /Å <sup>2</sup> )	38.13			37.88
Target defocus range (μm)	1.1-2.3			1.1-2.0
Calibrated pixel size (Å)	0.72			0.72
Symmetry imposed	C1			C1
Collected movies (no.)	11,981			3,489
Initial particle images (no.)	5,201,261			1,211,666
Final particle images (no.)	189,916	66,665	91,966	163,771
Map resolution at FSC=0.143 (Å)	2.91	3.07	3.41	3.43
<b>Refinement</b>				
Initial model used	otoferlin (216-1931)	otoferlin (216-1931)	otoferlin (216-1931)	otoferlin (216-1931)
Model resolution (Å)	3.5	3.1	3.6	3.5
Model resolution at FSC=0.5 (Å)	3.51	4.03	3.7	4.09
Map sharpening B factor (Å <sup>2</sup> )	-95.0	-60.7	-75.58	-113.7
<b>Model composition</b>				
Non-hydrogen atoms	11,977	12,199	11,944	10,297
Protein residues	1,489	1,517	1,483	1,284
Ligands	-	-	-	-
Waters	-	-	-	-
Ions	7x Ca <sup>2+</sup>	9x Ca <sup>2+</sup>	5x Ca <sup>2+</sup>	-
<b>B factors (Å<sup>2</sup>)</b>				
Protein (min/max/mean)	35.86/247.35/112.52	30.35/213.45/103.75	26.06/241.84/102.82	84.0/325.01/156.15
Ligand (min/max/mean)	62.47/224.90/146.67	97.01/155.05/126.82	63.30/176.17/123.57	-
Water	-	-	-	-
<b>R.m.s. deviations</b>				
Bond lengths (Å)	0.005	0.005	0.004	0.004
Bond angles (°)	0.976	1.060	0.951	1.031
<b>Validation</b>				
Molprobity score	1.67	1.82	1.47	1.59
Clashscore	3.20	4.55	3.08	2.88
Rotamer outliers (%)	2.66	2.16	1.60	1.76
Cβ outliers (%)	-	-	-	0.08
CaBLAM outliers (%)	1.57	2.81	1.51	2.54
<b>Ramachandran plot</b>				
Favored (%)	96.47	95.22	96.66	95.36
Allowed (%)	3.46	4.52	3.20	4.56
Disallowed (%)	0.07	0.27	0.14	0.08

**Table S3. List of patient mutations, their phenotypes and mapping on the otoferlin structure**

Nucleotide change	Amino acid change	Domain	Severity	Zygoty	Reference
c.650A>G	p.D217G	C <sub>2</sub> A-C <sub>2</sub> B linker	Mild	Comp het (p.A1802V)	(117)
c.1469C>A	p.P490Q	C <sub>2</sub> C	Profound	Comp het (p.I515T)	(118)
c.1544T>C	p.I515T	C <sub>2</sub> C	Profound	Comp het (p.P490Q)	(118)
c.1550T>C	p.L517P	C <sub>2</sub> C	Profound	Comp het (p.I1967del)	(119)
c.1841G>A	p.G614E	C <sub>2</sub> CD	Mild	Comp het (p.R1080P)	(120)
c.3127G>A	p.G1043S	C <sub>2</sub> D	Unreported	Hom	--
c.3239G>C	p.R1080P	C <sub>2</sub> D	Mild	Comp het (p.G614E)	(120)
c.4718T>C	p.I1573T	C <sub>2</sub> F	Mild to profound	Hom and Comp het (p. Ala1377Argfs*142)	(121–123)
c.4882C>A	p.P1628T	C <sub>2</sub> F (dsRBD-like)	Mild	Comp het (p.E1700G)	(124)
c.5332G>T	p.V1778F	C <sub>2</sub> G	Mild to moderate	Hom	(125)
c.5405C>T	p.A1802V	C <sub>2</sub> G	Mild	Comp het (p.D217G)	(117)
c.5524G>A	p.D1842N	C <sub>2</sub> G	Moderate	Het	(82)
c.5900_5902delTCA	p.I1967del	TM proximal	Mild to moderate, 15% speech perception	Comp het (p.L517P)	(119)
Abbreviations: Hom: homozygous, Comp het: compound heterozygous, Het: heterozygous					

**Table S4. Statistical analysis of electron tomography of *Otof*<sup>fDA</sup> mice.**

<b>N of RA-SVs</b>	
Wt ( <i>n</i> = 7 ribbons)	19.1 ± 2.2
<i>Otof</i> <sup>fDA</sup> ( <i>n</i> = 9 ribbons)	24.4 ± 1.6
<i>p</i>	> 0.05
Mice: <i>N</i> = 1 WT; <i>N</i> = 2 <i>Otof</i> <sup>fDA</sup>	Wilcoxon signed-rank test
<b>N of MP-SVs</b>	
Wt ( <i>n</i> = 7 ribbons)	14.9 ± 1.1
<i>Otof</i> <sup>fDA</sup> ( <i>n</i> = 9 ribbons)	16.7 ± 1.0
<i>p</i>	> 0.05
Mice: <i>N</i> = 1 WT; <i>N</i> = 2 <i>Otof</i> <sup>fDA</sup>	Wilcoxon signed-rank test
<b>Fraction of docked SV in MP-SV pool</b>	
Wt ( <i>n</i> = 7 ribbons)	0.334 ± 0.051
<i>Otof</i> <sup>fDA</sup> ( <i>n</i> = 9 ribbons)	0.298 ± 0.052
<i>p</i>	> 0.05
Mice: <i>N</i> = 1 WT; <i>N</i> = 2 <i>Otof</i> <sup>fDA</sup>	Wilcoxon signed-rank test
<b>Average distance of MP-SVs to the membrane</b>	
Wt ( <i>n</i> = 104 MP-SVs)	13.8 ± 1.4
<i>Otof</i> <sup>fDA</sup> ( <i>n</i> = 150 MP-SVs)	13.8 ± 1.3
<i>P</i>	> 0.05
Mice: <i>N</i> = 1 WT; <i>N</i> = 2 <i>Otof</i> <sup>fDA</sup>	Wilcoxon signed-rank test
<b>Average distance of docked SV to the PD</b>	
Wt ( <i>n</i> = 36 docked SVs)	25.4 ± 5.0
<i>Otof</i> <sup>fDA</sup> ( <i>n</i> = 150 docked SVs)	22.7 ± 4.3
<i>p</i>	> 0.05
Mice: <i>N</i> = 1 WT; <i>N</i> = 2 TDA KO	Wilcoxon signed-rank test

## Movie Legends

### **Movie S1. Cryo-EM maps of membrane-bound otoferlin (residues 216-1931).**

The final cryo-EM map of otoferlin (residues 216-1931) bound to an MSP2N2 lipid nanodisc has been coloured after the modelled domains. A low-pass filtered (to 8 Å) cryo-EM density map (grey) has been contoured around the high-resolution map of otoferlin.

### **Movie S2. The membrane-binding interfaces resolved in the otoferlin (216-1931)-nanodisc complex.**

The cryo-EM density map of otoferlin (216-1931) has been low-passed to 8 Å to enable the visualization of ordered protein-membrane contacts and is contoured (grey) around the final cryo-EM model. The resolved structural motifs of otoferlin are coloured.

### **Movie S3. Morphing between the lipid-free and nanodisc-bound structures of otoferlin.**

The two structures were superimposed based on the rigid C<sub>2</sub>C-C<sub>2</sub>D region and the movement of the otoferlin domains between the two models (morphing) were estimated in ChimeraX v.1.8.

### **Movie S4. Superposition of the lipid-free and nanodisc-bound structures of otoferlin (216-1931).**

The two cryo-EM structures of otoferlin were aligned based on the C<sub>2</sub>C-C<sub>2</sub>D region. The domains of otoferlin are colour-coded as in **Fig. 1**.



## REFERENCES AND NOTES

1. T. Moser, C. P. Grabner, F. Schmitz, Sensory processing at ribbon synapses in the retina and the cochlea. *Physiol. Rev.* **100**, 103–144 (2020).
2. M. A. Rutherford, H. Von Gersdorff, J. D. Goutman, Encoding sound in the cochlea: From receptor potential to afferent discharge. *J. Physiol.* **599**, 2527–2557 (2021).
3. S. L. Johnson, S. Safieddine, M. Mustapha, W. Marcotti, Hair cell afferent synapses: Function and dysfunction. *Cold Spring Harb. Perspect. Med.* **9**, a033175 (2019).
4. S. Safieddine, R. J. Wenthold, SNARE complex at the ribbon synapses of cochlear hair cells: Analysis of synaptic vesicle- and synaptic membrane-associated proteins. *Eur. J. Neurosci.* **11**, 803–812 (1999).
5. A. Brandt, J. Striessnig, T. Moser, CaV1.3 channels are essential for development and presynaptic activity of cochlear inner hair cells. *J. Neurosci.* **23**, 10832–10840 (2003).
6. I. Roux, S. Safieddine, R. Nouvian, M. Grati, M.-C. Simmler, A. Bahloul, I. Perfettini, M. Le Gall, P. Rostaing, G. Hamard, A. Triller, P. Avan, T. Moser, C. Petit, Otoferlin, defective in a human deafness form, is essential for exocytosis at the auditory ribbon synapse. *Cell* **127**, 277–289 (2006).
7. R. P. Seal, O. Akil, E. Yi, C. M. Weber, L. Grant, J. Yoo, A. Clause, K. Kandler, J. L. Noebels, E. Glowatzki, L. R. Lustig, R. H. Edwards, Sensorineural deafness and seizures in mice lacking vesicular glutamate transporter 3. *Neuron* **57**, 263–275 (2008).
8. N. Strenzke, S. Chanda, C. Kopp-Scheinpflug, D. Khimich, K. Reim, A. V. Bulankina, A. Neef, F. Wolf, N. Brose, M. A. Xu-Friedman, T. Moser, Complexin-I is required for high-fidelity transmission at the endbulb of held auditory synapse. *J. Neurosci.* **29**, 7991–8004 (2009).
9. R. C. Uthaiiah, A. J. Hudspeth, Molecular anatomy of the hair cell's ribbon synapse. *J. Neurosci.* **30**, 12387–12399 (2010).

10. E. Reisinger, C. Bresee, J. Neef, R. Nair, K. Reuter, A. Bulankina, R. Nouvian, M. Koch, J. Bückers, L. Kastrup, I. Roux, C. Petit, S. W. Hell, N. Brose, J.-S. Rhee, S. Kügler, J. V. Brigande, T. Moser, Probing the functional equivalence of otoferlin and synaptotagmin 1 in exocytosis. *J. Neurosci.* **31**, 4886–4895 (2011).
11. R. Nouvian, J. Neef, A. V. Bulankina, E. Reisinger, T. Pangršič, T. Frank, S. Sikorra, N. Brose, T. Binz, T. Moser, Exocytosis at the hair cell ribbon synapse apparently operates without neuronal SNARE proteins. *Nat. Neurosci.* **14**, 411–413 (2011).
12. C. Vogl, B. H. Cooper, J. Neef, S. M. Wojcik, K. Reim, E. Reisinger, N. Brose, J.-S. Rhee, T. Moser, C. Wichmann, Unconventional molecular regulation of synaptic vesicle replenishment in cochlear inner hair cells. *J. Cell Sci.* **128**, 638–644 (2015).
13. A. P. Cepeda, M. Ninov, J. Neef, I. Parfentev, K. Kusch, E. Reisinger, R. Jahn, T. Moser, H. Urlaub, Proteomic analysis reveals the composition of glutamatergic organelles of auditory inner hair cells. *Mol. Cell. Proteomics* **23**, 100704 (2024).
14. J. Rizo, Molecular mechanisms underlying neurotransmitter release.. *Annu. Rev. Biophys.* **51**, 377–408 (2022).
15. R. Jahn, D. C. Cafiso, L. K. Tamm, Mechanisms of SNARE proteins in membrane fusion. *Nat. Rev. Mol. Cell Biol.* **25**, 101–118 (2024).
16. C. Calvet, T. Peineau, N. Benamer, M. Cornille, A. Lelli, B. Plion, G. Lahlou, J. Fanchette, S. Nouaille, J. B. de Monvel, A. Estivalet, P. Jean, V. Michel, M. Sachse, N. Michalski, P. Avan, C. Petit, D. Dulon, S. Safieddine, The SNARE protein SNAP-25 is required for normal exocytosis at auditory hair cell ribbon synapses. *iScience* **25**, 105628 (2022).
17. T. Moser, A. Starr, Auditory neuropathy—Neural and synaptic mechanisms. *Nat. Rev. Neurol.* **12**, 135–149 (2016).
18. S. Yasunaga, M. Grati, M. Cohen-Salmon, A. El-Amraoui, M. Mustapha, N. Salem, E. El-Zir, J. Loiselet, C. Petit, A mutation in OTOF, encoding otoferlin, a FER-1-like protein, causes DFNB9, a nonsyndromic form of deafness. *Nat. Genet.* **21**, 363–369 (1999).

19. S. M. Baig, A. Koschak, A. Lieb, M. Gebhart, C. Dafinger, G. Nürnberg, A. Ali, I. Ahmad, M. J. Sinnegger-Brauns, N. Brandt, J. Engel, M. E. Mangoni, M. Farooq, H. U. Khan, P. Nürnberg, J. Striessnig, H. J. Bolz, Loss of Ca(v)1.3 (CACNA1D) function in a human channelopathy with bradycardia and congenital deafness. *Nat. Neurosci.* **14**, 77–84 (2011).
20. I. Schrauwen, S. Helfmann, A. Inagaki, F. Predoehl, M. A. Tabatabaieifar, M. M. Picher, M. Sommen, C. Z. Seco, J. Oostrik, H. Kremer, A. Dheedene, C. Claes, E. Franssen, M. H. Chaleshtori, P. Coucke, A. Lee, T. Moser, G. Van Camp, A mutation in CABP2, expressed in cochlear hair cells, causes autosomal-recessive hearing impairment. *Am. J. Hum. Genet.* **91**, 636–645 (2012).
21. J. Platzter, J. Engel, A. Schrott-Fischer, K. Stephan, S. Bova, H. Chen, H. Zheng, J. Striessnig, Congenital deafness and sinoatrial node dysfunction in mice lacking class D L-type  $\text{Ca}^{2+}$  channels. *Cell* **102**, 89–97 (2000).
22. A. Brandt, D. Khimich, T. Moser, Few CaV1.3 channels regulate the exocytosis of a synaptic vesicle at the hair cell ribbon synapse. *J. Neurosci.* **25**, 11577–11585 (2005).
23. T. Pangršič, M. Gabrielaitis, S. Michanski, B. Schwaller, F. Wolf, N. Strenzke, T. Moser, EF-hand protein  $\text{Ca}^{2+}$  buffers regulate  $\text{Ca}^{2+}$  influx and exocytosis in sensory hair cells. *Proc. Natl. Acad. Sci. U.S.A.* **112**, E1028–E1037 (2015).
24. L. M. Jaime Tobón, T. Moser,  $\text{Ca}^{2+}$  regulation of glutamate release from inner hair cells of hearing mice. *Proc. Natl. Acad. Sci. U.S.A.* **120**, e2311539120 (2023).
25. T. Pangrsic, E. Reisinger, T. Moser, Otoferlin: A multi-C2 domain protein essential for hearing. *Trends Neurosci.* **35**, 671–680 (2012).
26. S. T. Cooper, P. L. McNeil, Membrane repair: Mechanisms and pathophysiology. *Physiol. Rev.* **95**, 1205–1240 (2015).
27. T. Pangrsic, L. Lasarow, K. Reuter, H. Takago, M. Schwander, D. Riedel, T. Frank, L. M. Tarantino, J. S. Bailey, N. Strenzke, N. Brose, U. Müller, E. Reisinger, T. Moser, Hearing

requires otoferlin-dependent efficient replenishment of synaptic vesicles in hair cells. *Nat. Neurosci.* **13**, 869–876 (2010).

28. N. H. Revelo, D. Kamin, S. Truckenbrodt, A. B. Wong, K. Reuter-Jessen, E. Reisinger, T. Moser, S. O. Rizzoli, A new probe for super-resolution imaging of membranes elucidates trafficking pathways. *J. Cell Biol.* **205**, 591–606 (2014).
29. S. Jung, T. Maritzen, C. Wichmann, Z. Jing, A. Neef, N. H. Revelo, H. Al-Moyed, S. Meese, S. M. Wojcik, I. Panou, H. Bulut, P. Schu, R. Ficner, E. Reisinger, S. O. Rizzoli, J. Neef, N. Strenzke, V. Haucke, T. Moser, Disruption of adaptor protein 2 $\mu$  (AP-2 $\mu$ ) in cochlear hair cells impairs vesicle reloading of synaptic release sites and hearing. *EMBO J.* **34**, 2686–2702 (2015).
30. C. P. Johnson, E. R. Chapman, Otoferlin is a calcium sensor that directly regulates SNARE-mediated membrane fusion. *J. Cell Biol.* **191**, 187–197 (2010).
31. N. Michalski, J. D. Goutman, S. M. Auclair, J. Boutet de Monvel, M. Tertrais, A. Emptoz, A. Parrin, S. Nouaille, M. Guillon, M. Sachse, D. Ciric, A. Bahloul, J.-P. Hardelin, R. B. Sutton, P. Avan, S. S. Krishnakumar, J. E. Rothman, D. Dulon, S. Safieddine, C. Petit, Otoferlin acts as a Ca<sup>2+</sup> sensor for vesicle fusion and vesicle pool replenishment at auditory hair cell ribbon synapses. *eLife* **6**, e31013 (2017).
32. R. Fernández-Chacón, A. Königstorfer, S. H. Gerber, J. García, M. F. Matos, C. F. Stevens, N. Brose, J. Rizo, C. Rosenmund, T. C. Südhof, Synaptotagmin I functions as a calcium regulator of release probability. *Nature* **410**, 41–49 (2001).
33. O. Kochubey, R. Schneggenburger, Synaptotagmin increases the dynamic range of synapses by driving Ca<sup>2+</sup>-evoked release and by clamping a near-linear remaining Ca<sup>2+</sup> sensor. *Neuron* **69**, 736–748 (2011).
34. H. Chen, M. Monga, Q. Fang, L. Slitin, J. Neef, S. S. Chepurwar, R. C. M. Netto, K. Lezirovitz, A. Tabith, F. Benseler, N. Brose, K. Kusch, C. Wichmann, N. Strenzke, B. Vona, J. Preobraschenski, T. Moser, Ca<sup>2+</sup> binding to the C<sub>2</sub>E domain of otoferlin is required for hair cell exocytosis and hearing. *Protein Cell* **15**, 305–312 (2024).



35. D. Beutner, T. Voets, E. Neher, T. Moser, Calcium dependence of exocytosis and endocytosis at the cochlear inner hair cell afferent synapse. *Neuron* **29**, 681–690 (2001).
36. C. Vogl, I. Panou, G. Yamanbaeva, C. Wichmann, S. J. Mangosing, F. Vilardi, A. A. Indzhukulian, T. Pangršič, R. Santarelli, M. Rodriguez-Ballesteros, T. Weber, S. Jung, E. Cardenas, X. Wu, S. M. Wojcik, K. Y. Kwan, I. Del Castillo, B. Schwappach, N. Strenzke, D. P. Corey, S.-Y. Lin, T. Moser, Tryptophan-rich basic protein (WRB) mediates insertion of the tail-anchored protein otoferlin and is required for hair cell exocytosis and hearing. *EMBO J.* **35**, 2536–2552 (2016).
37. N. Strenzke, R. Chakrabarti, H. Al-Moyed, A. Müller, G. Hoch, T. Pangrsic, G. Yamanbaeva, C. Lenz, K.-T. Pan, E. Auge, R. Geiss-Friedlander, H. Urlaub, N. Brose, C. Wichmann, E. Reisinger, Hair cell synaptic dysfunction, auditory fatigue and thermal sensitivity in otoferlin Ile515Thr mutants. *EMBO J.* **35**, 2519–2535 (2016).
38. S. V. Duncker, C. Franz, S. Kuhn, U. Schulte, D. Campanelli, N. Brandt, B. Hirt, B. Fakler, N. Blin, P. Ruth, J. Engel, W. Marcotti, U. Zimmermann, M. Knipper, Otoferlin couples to clathrin-mediated endocytosis in mature cochlear inner hair cells. *J. Neurosci.* **33**, 9508–9519 (2013).
39. M. Tertrais, Y. Bouleau, A. Emptoz, S. Belleudy, R. B. Sutton, C. Petit, S. Safieddine, D. Dulon, Viral transfer of mini-otoferlins partially restores the fast component of exocytosis and uncovers ultrafast endocytosis in auditory hair cells of otoferlin knock-out mice. *J. Neurosci.* **39**, 3394–3411 (2019).
40. N. Hams, M. Padmanarayana, W. Qiu, C. P. Johnson, Otoferlin is a multivalent calcium-sensitive scaffold linking SNAREs and calcium channels. *Proc. Natl. Acad. Sci. U.S.A.* **114**, 8023–8028 (2017).
41. S. Helfmann, P. Neumann, K. Tittmann, T. Moser, R. Ficner, E. Reisinger, The crystal structure of the C<sub>2</sub>A domain of otoferlin reveals an unconventional top loop region. *J. Mol. Biol.* **406**, 479–490 (2011).

42. A. H. Shaib, A. A. Chouaib, R. Chowdhury, J. Altendorf, D. Mihaylov, C. Zhang, D. Krah, V. Imani, R. K. W. Spencer, S. V. Georgiev, N. Mougios, M. Monga, S. Reshetniak, T. Mimoso, H. Chen, P. Fatehbasharzad, D. Crzan, K.-A. Saal, M. M. Alawieh, N. Alawar, J. Eilts, J. Kang, A. Soleimani, M. Müller, C. Pape, L. Alvarez, C. Trenkwalder, B. Mollenhauer, T. F. Outeiro, S. Köster, J. Preobraschenski, U. Becherer, T. Moser, E. S. Boyden, A. R. Aricescu, M. Sauer, F. Opazo, S. O. Rizzoli, One-step nanoscale expansion microscopy reveals individual protein shapes. *Nat. Biotechnol.*, **43**, 1539–1547 (2025).
43. H.-L. Huang, G. Grandinetti, S. M. Heissler, K. Chinthalapudi, Cryo-EM structures of the membrane repair protein dysferlin. *Nat. Commun.* **15**, 9650 (2024).
44. C. Cretu, A. Chernev, C. Z. Kibédi Szabó, V. Pena, H. Urlaub, T. Moser, J. Preobraschenski, Structural insights into lipid membrane binding by human ferlins. *EMBO J.* **44**, 3926–3958 (2025).
45. B. Vona, A. Rad, E. Reisinger, The many faces of DFNB9: Relating OTOF variants to hearing impairment. *Genes* **11**, 1411 (2020).
46. H. Al-Moyed, A. P. Cepeda, S. Jung, T. Moser, S. Kügler, E. Reisinger, A dual-AAV approach restores fast exocytosis and partially rescues auditory function in deaf otoferlin knock-out mice. *EMBO Mol. Med.* **11**, e9396 (2019).
47. O. Akil, F. Dyka, C. Calvet, A. Emptoz, G. Lahlou, S. Nouaille, J. B. de Monvel, J.-P. Hardelin, W. W. Hauswirth, P. Avan, C. Petit, S. Safieddine, L. R. Lustig, Dual AAV-mediated gene therapy restores hearing in a DFNB9 mouse model. *Proc. Natl. Acad. Sci. U.S.A.* **116**, 4496–4501 (2019).
48. J. Lv, H. Wang, X. Cheng, Y. Chen, D. Wang, L. Zhang, Q. Cao, H. Tang, S. Hu, K. Gao, M. Xun, J. Wang, Z. Wang, B. Zhu, C. Cui, Z. Gao, L. Guo, S. Yu, L. Jiang, Y. Yin, J. Zhang, B. Chen, W. Wang, R. Chai, Z.-Y. Chen, H. Li, Y. Shu, AAV1-hOTOF gene therapy for autosomal recessive deafness 9: A single-arm trial. *Lancet* **403**, 2317–2325 (2024).

49. J. Qi, F. Tan, L. Zhang, L. Lu, S. Zhang, Y. Zhai, Y. Lu, X. Qian, W. Dong, Y. Zhou, Z. Zhang, X. Yang, L. Jiang, C. Yu, J. Liu, T. Chen, L. Wu, C. Tan, S. Sun, H. Song, Y. Shu, L. Xu, X. Gao, H. Li, R. Chai, AAV-mediated gene therapy restores hearing in patients with DFNB9 deafness. *Adv. Sci.* **11**, e2306788 (2024).
50. H. Wang, Y. Chen, J. Lv, X. Cheng, Q. Cao, D. Wang, L. Zhang, B. Zhu, M. Shen, C. Xu, M. Xun, Z. Wang, H. Tang, S. Hu, C. Cui, L. Jiang, Y. Yin, L. Guo, Y. Zhou, L. Han, Z. Gao, J. Zhang, S. Yu, K. Gao, J. Wang, B. Chen, W. Wang, Z.-Y. Chen, H. Li, Y. Shu, Bilateral gene therapy in children with autosomal recessive deafness 9: Single-arm trial results. *Nat. Med.* **30**, 1898–1904 (2024).
51. H. Liu, H. Liu, L. Wang, L. Song, G. Jiang, Q. Lu, T. Yang, H. Peng, R. Cai, X. Zhao, T. Zhao, H. Wu, Cochlear transcript diversity and its role in auditory functions implied by an otoferlin short isoform. *Nat. Commun.* **14**, 3085 (2023).
52. K. S. Cannon, R. D. Sarsam, T. Tadamrongwanish, K. Zhang, R. W. Baker, Lipid nanodiscs as a template for high-resolution cryo-EM structures of peripheral membrane proteins. *J. Struct. Biol.* **215**, 107989 (2023).
53. H. Chen, Q. Fang, F. Benseler, N. Brose, T. Moser, Probing the role of the C<sub>2</sub>F domain of otoferlin. *Front. Mol. Neurosci.* **16**, 1299509 (2023).
54. M. Padmanarayana, N. Hams, L. C. Speight, E. J. Petersson, R. A. Mehl, C. P. Johnson, Characterization of the lipid binding properties of otoferlin reveals specific interactions between PI(4,5)P<sub>2</sub> and the C<sub>2</sub>C and C<sub>2</sub>F domains. *Biochemistry* **53**, 5023–5033 (2014).
55. N. J. Marty, C. L. Holman, N. Abdullah, C. P. Johnson, The C<sub>2</sub> domains of otoferlin, dysferlin, and myoferlin alter the packing of lipid bilayers. *Biochemistry* **52**, 5585–5592 (2013).
56. E. Neher, N. Brose, Dynamically primed synaptic vesicle states: Key to understand synaptic short-term plasticity. *Neuron* **100**, 1283–1291 (2018).
57. T. Moser, D. Beutner, Kinetics of exocytosis and endocytosis at the cochlear inner hair cell afferent synapse of the mouse. *Proc. Natl. Acad. Sci. U.S.A.* **97**, 883–888 (2000).

58. J. D. Goutman, E. Glowatzki, Time course and calcium dependence of transmitter release at a single ribbon synapse. *Proc. Natl. Acad. Sci. U.S.A.* **104**, 16341–16346 (2007).
59. L. M. Jaime Tobón, T. Moser, Bridging the gap between presynaptic hair cell function and neural sound encoding. *eLife* **12**, RP93749 (2024).
60. D. Bansal, K. Miyake, S. S. Vogel, S. Groh, C.-C. Chen, R. Williamson, P. L. McNeil, K. P. Campbell, Defective membrane repair in dysferlin-deficient muscular dystrophy. *Nature* **423**, 168–172 (2003).
61. S. Jo, T. Kim, V. G. Iyer, W. Im, CHARMM-GUI: A web-based graphical user interface for CHARMM. *J. Comput. Chem.* **29**, 1859–1865 (2008).
62. J. Ruel, S. Emery, R. Nouvian, T. Bersot, B. Amilhon, J. M. Van Rybroek, G. Rebillard, M. Lenoir, M. Eybalin, B. Delprat, T. A. Sivakumaran, B. Giros, S. El Mestikawy, T. Moser, R. J. H. Smith, M. M. Lesperance, J.-L. Puel, Impairment of SLC17A8 encoding vesicular glutamate transporter-3, VGLUT3, underlies nonsyndromic deafness DFNA25 and inner hair cell dysfunction in null mice. *Am. J. Hum. Genet.* **83**, 278–292 (2008).
63. D. Khimich, R. Nouvian, R. Pujol, S. T. Dieck, A. Egner, E. D. Gundelfinger, T. Moser, Hair cell synaptic ribbons are essential for synchronous auditory signalling. *Nature* **434**, 889–894 (2005).
64. T. Moser, “Presynaptic physiology of cochlear inner hair cells,” in *The Senses: A Comprehensive Reference* (Elsevier, 2020), pp. 441–467;  
<https://linkinghub.elsevier.com/retrieve/pii/B9780128093245241850>.
65. Y. Hua, X. Ding, H. Wang, F. Wang, Y. Lu, J. Neef, Y. Gao, T. Moser, H. Wu, Electron microscopic reconstruction of neural circuitry in the cochlea. *Cell Rep.* **34**, 108551 (2021).
66. P. Heil, H. Neubauer, D. R. F. Irvine, M. Brown, Spontaneous activity of auditory-nerve fibers: insights into stochastic processes at ribbon synapses. *J. Neurosci.* **27**, 8457–8474 (2007).



67. B. N. Buran, N. Strenzke, A. Neef, E. D. Gundelfinger, T. Moser, M. C. Liberman, Onset coding is degraded in auditory nerve fibers from mutant mice lacking synaptic ribbons. *J. Neurosci.* **30**, 7587–7597 (2010).
68. M. Avissar, J. H. Wittig, J. C. Saunders, T. D. Parsons, Refractoriness enhances temporal coding by auditory nerve fibers. *J. Neurosci.* **33**, 7681–7690 (2013).
69. T. Frank, M. A. Rutherford, N. Strenzke, A. Neef, T. Pangršič, D. Khimich, A. Fejtova, E. D. Gundelfinger, M. C. Liberman, B. Harke, K. E. Bryan, A. Lee, A. Egner, D. Riedel, T. Moser, Bassoon and the synaptic ribbon organize  $\text{Ca}^{2+}$  channels and vesicles to add release sites and promote refilling. *Neuron* **68**, 724–738 (2010).
70. A. Neef, D. Khimich, P. Pirih, D. Riedel, F. Wolf, T. Moser, Probing the mechanism of exocytosis at the hair cell ribbon synapse. *J. Neurosci.* **27**, 12933–12944 (2007).
71. C. P. Grabner, T. Moser, Individual synaptic vesicles mediate stimulated exocytosis from cochlear inner hair cells. *Proc. Natl. Acad. Sci. U.S.A.* **115**, 12811–12816 (2018).
72. B. D. Winegar, J. B. Lansman, Voltage-dependent block by zinc of single calcium channels in mouse myotubes. *J. Physiol.* **425**, 563–578 (1990).
73. M. Beurg, N. Michalski, S. Safieddine, Y. Bouleau, R. Schneggenburger, E. R. Chapman, C. Petit, D. Dulon, Control of exocytosis by synaptotagmins and otoferlin in auditory hair cells. *J. Neurosci.* **30**, 13281–13290 (2010).
74. Y. Lai, U. B. Choi, J. Leitz, H. J. Rhee, C. Lee, B. Altas, M. Zhao, R. A. Pfuetzner, A. L. Wang, N. Brose, J. S. Rhee, A. T. Brunger, Molecular mechanisms of synaptic vesicle priming by Munc13 and Munc18. *Neuron* **95**, 591–607.e10 (2017).
75. B. Quade, M. Camacho, X. Zhao, M. Orlando, T. Trimbuch, J. Xu, W. Li, D. Nicastro, C. Rosenmund, J. Rizo, Membrane bridging by Munc13–1 is crucial for neurotransmitter release. *eLife* **8**, e42806 (2019).

76. M. Verhage, A. S. Maia, J. J. Plomp, A. B. Brussaard, J. H. Heeroma, H. Vermeer, R. F. Toonen, R. E. Hammer, T. K. van den Berg, M. Missler, H. J. Geuze, T. C. Südhof, Synaptic assembly of the brain in the absence of neurotransmitter secretion. *Science* **287**, 864–869 (2000).
77. F. Varoqueaux, A. Sigler, J.-S. Rhee, N. Brose, C. Enk, K. Reim, C. Rosenmund, Total arrest of spontaneous and evoked synaptic transmission but normal synaptogenesis in the absence of Munc13-mediated vesicle priming. *Proc. Natl. Acad. Sci. U.S.A.* **99**, 9037–9042 (2002).
78. A. T. Brunger, J. Leitz, The core complex of the  $\text{Ca}^{2+}$ -triggered presynaptic fusion machinery. *J. Mol. Biol.* **435**, 167853 (2023).
79. Q. Zhou, P. Zhou, A. L. Wang, D. Wu, M. Zhao, T. C. Südhof, A. T. Brunger, The primed SNARE-complexin-synaptotagmin complex for neuronal exocytosis. *Nature* **548**, 420–425 (2017).
80. M. Schwander, A. Sczaniecka, N. Grillet, J. S. Bailey, M. Avenarius, H. Najmabadi, B. M. Steffy, G. C. Federe, E. A. Lagler, R. Banan, R. Hice, L. Grabowski-Boase, E. M. Keithley, A. F. Ryan, G. D. Housley, T. Wiltshire, R. J. H. Smith, L. M. Tarantino, U. Müller, A forward genetics screen in mice identifies recessive deafness traits and reveals that pejvakin is essential for outer hair cell function. *J. Neurosci.* **27**, 2163–2175 (2007).
81. R. Chakrabarti, S. Michanski, C. Wichmann, Vesicle sub-pool organization at inner hair cell ribbon synapses. *EMBO Rep.* **19**, e44937 (2018).
82. T. Matsunaga, H. Mutai, S. Kunishima, K. Namba, N. Morimoto, Y. Shinjo, Y. Arimoto, Y. Kataoka, T. Shintani, N. Morita, T. Sugiuchi, S. Masuda, A. Nakano, H. Taiji, K. Kaga, A prevalent founder mutation and genotype-phenotype correlations of OTOF in Japanese patients with auditory neuropathy. *Clin. Genet.* **82**, 425–432 (2012).
83. N. Karagulyan, A. Thirumalai, S. Michanski, Y. Qi, Q. Fang, H. Wang, N. J. Ortner, J. Striessnig, N. Strenzke, C. Wichmann, Y. Hua, T. Moser, Gating of hair cell  $\text{Ca}^{2+}$  channels governs the activity of cochlear neurons. *Sci. Adv.* **11**, eadu7898 (2025).

84. J. Schmitzová, C. Cretu, C. Dienemann, H. Urlaub, V. Pena, Structural basis of catalytic activation in human splicing. *Nature* **617**, 842–850 (2023).
85. C. Cretu, A. A. Agrawal, A. Cook, C. L. Will, P. Fekkes, P. G. Smith, R. Lührmann, N. Larsen, S. Buonamici, V. Pena, Structural basis of splicing modulation by antitumor macrolide compounds. *Mol. Cell* **70**, 265–273.e8 (2018).
86. C. Cretu, P. Gee, X. Liu, A. Agrawal, T.-V. Nguyen, A. K. Ghosh, A. Cook, M. Jurica, N. A. Larsen, V. Pena, Structural basis of intron selection by U2 snRNP in the presence of covalent inhibitors. *Nat. Commun.* **12**, 4491 (2021).
87. C. Cretu, J. Schmitzová, A. Ponce-Salvatierra, O. Dybkov, E. I. De Laurentiis, K. Sharma, C. L. Will, H. Urlaub, R. Lührmann, V. Pena, Molecular architecture of SF3b and structural consequences of its cancer-related mutations. *Mol. Cell* **64**, 307–319 (2016).
88. D. S. Brandt, M. D. Coffman, J. J. Falke, J. D. Knight, Hydrophobic contributions to the membrane docking of Synaptotagmin 7 C2A domain: Mechanistic contrast between isoforms 1 and 7. *Biochemistry* **51**, 7654–7664 (2012).
89. D. Kimanius, K. Jamali, M. E. Wilkinson, S. Lövestam, V. Velazhahan, T. Nakane, S. H. W. Scheres, Data-driven regularization lowers the size barrier of cryo-EM structure determination. *Nat Methods* **21**, 1216–1221 (2024).
90. A. J. Jakobi, M. Wilmanns, C. Sachse, Model-based local density sharpening of cryo-EM maps. *eLife* **6**, e27131 (2017).
91. J. Jumper, R. Evans, A. Pritzel, T. Green, M. Figurnov, O. Ronneberger, K. Tunyasuvunakool, R. Bates, A. Židek, A. Potapenko, A. Bridgland, C. Meyer, S. A. A. Kohl, A. J. Ballard, A. Cowie, B. Romera-Paredes, S. Nikolov, R. Jain, J. Adler, T. Back, S. Petersen, D. Reiman, E. Clancy, M. Zielinski, M. Steinegger, M. Pacholska, T. Berghammer, S. Bodenstein, D. Silver, O. Vinyals, A. W. Senior, K. Kavukcuoglu, P. Kohli, D. Hassabis, Highly accurate protein structure prediction with AlphaFold. *Nature* **596**, 583–589 (2021).

92. T. I. Croll, ISOLDE: A physically realistic environment for model building into low-resolution electron-density maps. *Acta Crystallogr. D Struct. Biol.* **74**, 519–530 (2018).
93. P. Emsley, K. Cowtan, Coot: Model-building tools for molecular graphics. *Acta Crystallogr. D Biol. Crystallogr.* **60**, 2126–2132 (2004).
94. P. V. Afonine, B. K. Poon, R. J. Read, O. V. Sobolev, T. C. Terwilliger, A. Urzhumtsev, P. D. Adams, Real-space refinement in PHENIX for cryo-EM and crystallography. *Acta Crystallogr. D Struct. Biol.* **74**, 531–544 (2018).
95. R. D. Oeffner, T. I. Croll, C. Millán, B. K. Poon, C. J. Schlicksup, R. J. Read, T. C. Terwilliger, Putting AlphaFold models to work with phenix.process\_predicted\_model and ISOLDE. *Acta Crystallogr. D Struct. Biol.* **78**, 1303–1314 (2022).
96. K. Yamashita, C. M. Palmer, T. Burnley, G. N. Murshudov, Cryo-EM single-particle structure refinement and map calculation using Servalcat. *Acta Crystallogr. D Struct. Biol.* **77**, 1282–1291 (2021).
97. E. Krissinel, K. Henrick, Inference of macromolecular assemblies from crystalline state. *J. Mol. Biol.* **372**, 774–797 (2007).
98. M. Lindau, E. Neher, Patch-clamp techniques for time-resolved capacitance measurements in single cells. *Pflügers Arch.* **411**, 137–146 (1988).
99. Z. Jing, M. A. Rutherford, H. Takago, T. Frank, A. Fejtova, D. Khimich, T. Moser, N. Strenzke, Disruption of the presynaptic cytomatrix protein bassoon degrades ribbon anchorage, multiquantal release, and sound encoding at the hair cell afferent synapse. *J. Neurosci.* **33**, 4456–4467 (2013).
100. A. M. Taberner, M. C. Liberman, Response properties of single auditory nerve fibers in the mouse. *J. Neurophysiol.* **93**, 557–569 (2005).

101. A. B. Wong, M. A. Rutherford, M. Gabrielaitis, T. Pangršič, F. Göttfert, T. Frank, S. Michanski, S. Hell, F. Wolf, C. Wichmann, T. Moser, Developmental refinement of hair cell synapses tightens the coupling of  $\text{Ca}^{2+}$  influx to exocytosis. *EMBO J.* **33**, 247–264 (2014).
102. P. Jean, D. L. de la Morena, S. Michanski, L. M. J. Tobón, R. Chakrabarti, M. M. Picher, J. Neef, S. Jung, M. Gültas, S. Maxeiner, A. Neef, C. Wichmann, N. Strenzke, C. Grabner, T. Moser, The synaptic ribbon is critical for sound encoding at high rates and with temporal precision. *eLife* **7**, e29275 (2018).
103. D. N. Mastronarde, Automated electron microscope tomography using robust prediction of specimen movements. *J. Struct. Biol.* **152**, 36–51 (2005).
104. J. R. Kremer, D. N. Mastronarde, J. R. McIntosh, Computer visualization of three-dimensional image data using IMOD. *J. Struct. Biol.* **116**, 71–76 (1996).
105. S. Muth, F. Moschref, L. Freckmann, S. Mutschall, I. Hojas-Garcia-Plaza, J. N. Bahr, A. Petrovic, T. T. Do, V. Schwarze, A. Archit, K. Weyand, S. Michanski, L. Maus, C. Imig, N. Brose, C. Wichmann, R. Fernandez-Busnadiego, T. Moser, S. O. Rizzoli, B. H. Cooper, C. Pape, SynapseNet: Deep learning for automatic synapse reconstruction. *Mol. Biol. Cell*, mbcE24110519 (2025).
106. N. Sofroniew, T. Lambert, G. Bokota, J. Nunez-Iglesias, P. Sobolewski, A. Sweet, L. Gaifas, K. Evans, A. Burt, D. Doncila Pop, K. Yamauchi, M. Weber Mendonça, G. Buckley, W.-M. Vierdag, L. Royer, A. Can Solak, K. I. S. Harrington, J. Ahlers, D. Althviz Moré, O. Amsalem, A. Anderson, A. Annex, P. Boone, J. Bragantini, M. Bussonnier, C. Caporal, J. Eglinger, A. Eisenbarth, J. Freeman, C. Gohlke, K. Gunalan, H. Har-Gil, M. Harfouche, V. Hilsenstein, K. Hutchings, J. Lauer, G. Lichtner, Z. Liu, L. Liu, A. Lowe, L. Marconato, S. Martin, A. McGovern, L. Migas, N. Miller, H. Muñoz, J.-H. Müller, C. Nauroth-Kreß, D. Palecek, C. Pape, E. Perlman, K. Pevey, G. Peña-Castellanos, A. Pierré, D. Pinto, J. Rodríguez-Guerra, D. Ross, C. T. Russell, J. Ryan, G. Selzer, M. Smith, P. Smith, K. Sofiiuk, J. Soltwedel, D. Stansby, J. Vanaret, P. Wadhwa, M. Weigert, J. Windhager, P. Winston, R. Zhao, napari: A multi-dimensional image viewer for Python, version v0.5.5 (Zenodo, 2024); <https://doi.org/10.5281/zenodo.14427406>.

107. S. Krinner, T. Butola, S. Jung, C. Wichmann, T. Moser, RIM-binding protein 2 promotes a large number of CaV1.3 Ca<sup>2+</sup>-channels and contributes to fast synaptic vesicle replenishment at hair cell active zones. *Front. Cell Neurosci.* **11**, 334 (2017).
108. A. Zhang, H. Yu, C. Liu, C. Song, The Ca<sup>2+</sup> permeation mechanism of the ryanodine receptor revealed by a multi-site ion model. *Nat. Commun.* **11**, 922 (2020).
109. J. Huang, S. Rauscher, G. Nawrocki, T. Ran, M. Feig, B. L. de Groot, H. Grubmüller, A. D. MacKerell, CHARMM36m: An improved force field for folded and intrinsically disordered proteins. *Nat. Methods* **14**, 71–73 (2017).
110. M. J. Abraham, T. Murtola, R. Schulz, S. Páll, J. C. Smith, B. Hess, E. Lindahl, GROMACS: High performance molecular simulations through multi-level parallelism from laptops to supercomputers. *SoftwareX* **1–2**, 19–25 (2015).
111. G. Bussi, D. Donadio, M. Parrinello, Canonical sampling through velocity rescaling. *J. Chem. Phys.* **126**, 014101 (2007).
112. M. Bernetti, G. Bussi, Pressure control using stochastic cell rescaling. *J. Chem. Phys.* **153**, 114107 (2020).
113. B. Hess, P-LINCS: A parallel linear constraint solver for molecular simulation. *J. Chem. Theory Comput.* **4**, 116–122 (2008).
114. U. Essmann, L. Perera, M. L. Berkowitz, T. Darden, H. Lee, L. G. Pedersen, A smooth particle mesh Ewald method. *J. Chem. Phys.* **103**, 8577–8593 (1995).
115. E. Jurrus, D. Engel, K. Star, K. Monson, J. Brandi, L. E. Felberg, D. H. Brookes, L. Wilson, J. Chen, K. Liles, M. Chun, P. Li, D. W. Gohara, T. Dolinsky, R. Konecny, D. R. Koes, J. E. Nielsen, T. Head-Gordon, W. Geng, R. Krasny, G.-W. Wei, M. J. Holst, J. A. McCammon, N. A. Baker, Improvements to the APBS biomolecular solvation software suite. *Protein Sci.* **27**, 112–128 (2018).



116. F. B. Naughton, I. Alibay, J. Barnoud, E. Barreto-Ojeda, O. Beckstein, C. Bouysset, O. Cohen, R. J. Gowers, H. MacDermott-Opeskin, M. Matta, M. N. Melo, T. Reddy, L. Wang, Y. Zhuang, MDAnalysis 2.0 and beyond: Fast and interoperable, community driven simulation analysis. *Biophys. J.* **121**, 272a–273a (2022).
117. Y.-I. Iwasa, S.-Y. Nishio, A. Sugaya, Y. Kataoka, Y. Kanda, M. Taniguchi, K. Nagai, Y. Naito, T. Ikezono, R. Horie, Y. Sakurai, R. Matsuoka, H. Takeda, S. Abe, C. Kihara, T. Ishino, S.-Y. Morita, S. Iwasaki, M. Takahashi, T. Ito, Y. Arai, S.-I. Usami, OTOF mutation analysis with massively parallel DNA sequencing in 2,265 Japanese sensorineural hearing loss patients. *PLOS ONE* **14**, e0215932 (2019).
118. F. Mirghomizadeh, M. Pfister, F. Apaydin, C. Petit, S. Kupka, C. M. Pusch, H. P. Zenner, N. Blin, Substitutions in the conserved C2C domain of otoferlin cause DFNB9, a form of nonsyndromic autosomal recessive deafness. *Neurobiol. Dis.* **10**, 157–164 (2002).
119. Y. Wang, Y. Lu, J. Cheng, L. Zhang, D. Han, H. Yuan, Novel OTOF gene mutations identified using a massively parallel DNA sequencing technique in DFNB9 deafness. *Acta Otolaryngol.* **138**, 865–870 (2018).
120. J. Romanos, L. Kimura, M. L. Fávero, F. A. R. Izarra, M. T. B. de Mello Auricchio, A. C. Batisso, K. Lezirovitz, R. S. Abreu-Silva, R. C. Mingroni-Netto, Novel OTOF mutations in Brazilian patients with auditory neuropathy. *J. Hum. Genet.* **54**, 382–385 (2009).
121. M. Yildirim-Baylan, G. Bademci, D. Duman, H. Ozturkmen-Akay, S. Tokgoz-Yilmaz, M. Tekin, Evidence for genotype-phenotype correlation for OTOF mutations. *Int. J. Pediatr. Otorhinolaryngol.* **78**, 950–953 (2014).
122. C. L. Ford, W. J. Riggs, T. Quigley, O. P. Keifer, J. P. Whitton, V. Valayannopoulos, The natural history, clinical outcomes, and genotype–phenotype relationship of otoferlin-related hearing loss: A systematic, quantitative literature review. *Hum. Genet.* **142**, 1429–1449 (2023).
123. Y.-I. Iwasa, S.-Y. Nishio, H. Yoshimura, A. Sugaya, Y. Kataoka, Y. Maeda, Y. Kanda, K. Nagai, Y. Naito, H. Yamazaki, T. Ikezono, H. Matsuda, M. Nakai, R. Tona, Y. Sakurai, R.

Motegi, H. Takeda, M. Kobayashi, C. Kihara, T. Ishino, S.-Y. Morita, S. Iwasaki, M. Takahashi, S. Furutate, S.-I. Oka, T. Kubota, Y. Arai, Y. Kobayashi, D. Kikuchi, T. Shintani, N. Ogasawara, Y. Honkura, S. Izumi, M. Hyogo, Y. Ninoyu, M. Suematsu, J. Nakayama, N. Tsuchihashi, M. Okami, H. Sakata, H. Yoshihashi, T. Kobayashi, K. Kumakawa, T. Yoshida, T. Esaki, S.-I. Usami, Detailed clinical features and genotype-phenotype correlation in an OTOF-related hearing loss cohort in Japan. *Hum. Genet.* **141**, 865–875 (2022).

124. Y.-M. Zhu, Q. Li, X. Gao, Y.-F. Li, Y.-L. Liu, P. Dai, X.-P. Li, Familial temperature-sensitive auditory neuropathy: Distinctive clinical courses caused by variants of the OTOF gene. *Front. Cell Dev. Biol.* **9**, 732930 (2021).

125. A. M. Fedick, C. Jalas, A. Swaroop, E. E. Smouha, B. D. Webb, Identification of a novel pathogenic OTOF variant causative of nonsyndromic hearing loss with high frequency in the Ashkenazi Jewish population. *Appl. Clin. Genet.* **9**, 141–146 (2016).